

DEPARTMENT OF ELECTRICAL, ELECTRONIC, AND INFORMATION ENGINEERING "GUGLIELMO MARCONI" - DEI

SECOND CYCLE DEGREE

ELECTRONICS FOR INTELLIGENT SYSTEMS, BIG-DATA AND INTERNET OF THINGS INGEGNERIA ELETTRONICA

MODULATION PREDISTORTION TECHNIQUE FOR POLAR TRANSMITTER

Dissertation in LAB of Digital Electronics M

Supervisor Defended by

Prof. Davide Rossi Amirhossein Gerami

Co-Supervisors

Davide Bottamedi Stefano Marsili

Graduation Session / October/ 2025

Academic Year 2024/2025

Acknowledgement

I would like to express my deepest gratitude to my academic supervisor, Professor Davide Rossi, for his guidance and for giving me the opportunity to connect with Infineon Technologies, one of the leading companies in the field. His continuous support and encouragement were invaluable throughout the development of this thesis.

I am sincerely thankful to Davide Bottamedi and Stefano Marsili, my supervisors at Infineon, for their expertise, constructive feedback, and constant support during my work at the company. Their mentorship greatly enriched both my technical knowledge and professional growth.

I am profoundly grateful to my family. Although physically far from me during this journey, their unwavering love, encouragement, and belief in me have always been my strongest source of strength.

Finally, I wish to thank my friends Atena, Mahsa, and Mina, who stood by my side during the most challenging moments of being away from home. Their companionship and support made this journey far more bearable and meaningful.

Abstract

Orthogonal Frequency Division Multiplexing (OFDM) has become a cornerstone of modern wireless communication due to its robustness against multipath fading and high spectral efficiency. However, its practical deployment in polar transmitters is challenged by two critical impairments: the high peak-to-average power ratio (PAPR) of the amplitude component and abrupt discontinuities in the phase trajectory. These effects lead to power amplifier inefficiency, spectral regrowth, and degraded modulation accuracy.

This thesis investigates digital signal processing techniques for mitigating these impairments in the context of an all-digital polar modulator. The first part focuses on amplitude-domain Crest Factor Reduction (CFR) through a window-based peak cancellation approach, compared against amplitude clipping. MATLAB simulations demonstrate that the proposed CFR scheme achieves substantial PAPR reduction while maintaining lower error vector magnitude (EVM) degradation and superior compliance with the IEEE 802.11a spectral mask.

The second part addresses phase-domain discontinuities by introducing a phase smoothing algorithm based on excess redistribution across a short sample window. This method effectively suppresses instantaneous frequency spikes while preserving accumulated phase integrity. Performance evaluation highlights the trade-off between spectral containment and modulation accuracy, with an intermediate threshold providing the best balance.

Both algorithms were implemented in fixed-point arithmetic and translated into fully pipelined Verilog RTL architectures, including a CORDIC-based Cartesian-to-polar converter. Comprehensive MATLAB and RTL co-simulation confirmed bit-true equivalence, identical EVM and PAPR results, and full spectral compliance.

The outcomes of this work demonstrate that the integration of CFR and phase smoothing in a polar transmitter significantly improves spectral efficiency and power amplifier compatibility without compromising modulation fidelity.

Contents

1	Cha	apter	1: Introduction	7
	1.1	Bac	kground and Motivation	7
	1.2	Prol	blem Definition	8
	1.3	Obj	ectives and Scope	9
2	СН	APTE	R 2: Literature Review and Theoretical Background	10
	2.1	Qua	adrature Amplitude Modulation (QAM)	10
	2.2	OF	DM and IEEE 802.11a Overview	11
	2.2.	1	OFDM Principles	11
	2.2.	2	IEEE 802.11a PHY Structure	13
	2.3	Pola	ar Modulation and CORDIC	16
	2.3.	1	Polar Modulation vs. Conventional I/Q Transmitters	16
	2.3.	2	Envelope and Phase Separation	18
	2.3.	3	CORDIC Algorithm	19
	2.3.	4	Application of CORDIC in OFDM & PAPR	20
3	Cha	apter	3: Problem Definition & Analysis	21
	3.1	PAP	PR in OFDM	21
	3.1.	1	Mathematical Definition of PAPR	21
	3.1.	2	Origin of High PAPR in Multicarrier Systems	22
	3.1.	3	Impact on Power Amplifiers	23
	3.2	Pha	se Discontinuities and Instantaneous Frequency Spikes	24
	3.2.	1	Instantaneous Frequency Spikes	24
	3.2.	2	Impact on PLL and Spectrum	25
4	CH	APTE	R 4: Predistortion Techniques for Digital Polar Modulators	27
	4.1	PAP	PR Reduction Methods	28
	4.1.	1	Amplitude Clipping	28
	4.1.	2	Window-Based Crest Factor Reduction (Peak Windowing)	28
	4.2	Win	dow Functions for Peak Smoothing	29
	4.2.	1	Hamming Window Theory	29
	4.2.	2	FIR Filter Design	30

	4.3	Pha	se Smoothing Algorithm	. 31
5	Ch	apter	5: MATLAB Simulation Chain	. 32
	5.1	IEEE	E 802.11a Compliance	. 32
	5.1	I.1	Transmit Spectrum Mask	. 32
	5.1	1.2	Modulation Accuracy (EVM)	. 33
	5.2	MAT	TLAB Simulation	. 34
	5.2	2.1	Signal Generation	. 35
	5.2	2.2	Interpolation	. 36
	5.2	2.3	Amplitude Clipping and Peak Windowing	. 37
	5.2	2.4	Phase Smoothing	. 44
	5.3	Inte	grated CFR and Phase Smoothing Chain	. 52
6	CH	HAPTE	R 6: RTL Implementation of Key Modules	. 54
	6.1	RTL	Implementation of CORDIC	. 54
	6.1	1.1	Architecture and Block Diagram	. 54
	6.1	1.2	Input/Output Specification and Fixed-Point Representation	. 56
	6.2	RTL	Implementation of CFR	. 57
	6.2	2.1	Architecture and Block Diagram	. 57
	6.2	2.2	Input/Output Specification and Fixed-Point Representation	. 58
	6.3	RTL	Implementation of Phase Smoothing	. 59
	6.3	3.1	Architecture and Block Diagram	. 59
	6.3	3.2	Input/Output Specification and Fixed-Point Representation	. 60
7	CH	IAPTE	R 7: Results and Evaluation	. 61
	7.1	MAT	TLAB Results	. 61
	7.1	1.1	PAPR Reduction Methods – Amplitude Clipping and Peak Windowing	. 61
	7.1	1.2	Phase Smoothing	. 62
	7.1	1.3	Integration of Peak Windowing and Phase Smoothing	. 63
	7.2	RTL	Results	. 64
	7.3	MAT	TLAB vs RTL Comparison	. 66
8	CH	HAPTE	R 8: Conclusions and Future Work	. 68

9	Ref	erences	70
	8.2	Future Directions	69
	8.1	Summary of Achievements	68

1 Chapter 1: Introduction

1.1 Background and Motivation

Modern wireless systems demand ever-increasing data rates together with high spectral and power efficiency. Orthogonal frequency-division multiplexing (OFDM) is the de-facto multicarrier modulation in contemporary standards (e.g., IEEE 802.11a, LTE, 5G NR) because it is resilient to frequency-selective fading and enables efficient spectrum utilisation via simple per-subcarrier equalisation. A well-known drawback of OFDM is its high peak-to-average power ratio (PAPR), which forces the transmitter power amplifier (PA) to operate with substantial output back-off. The resulting reduction in PA efficiency is problematic for battery-powered devices and for high-throughput infrastructure nodes.

Polar modulation has emerged as a promising transmitter architecture to address PA efficiency limitations. By decomposing the complex baseband signal into envelope (magnitude) and phase components, polar transmitters allow the use of highly efficient, nonlinear or saturated PAs while still achieving overall linearity after recombination. This decomposition is especially attractive for all-digital transmitter implementations targeting advanced wireless standards.

However, polar architectures introduce their own impairments. The envelope and phase paths must be precisely time-aligned; furthermore, the discrete-time phase sequence often exhibits abrupt wraps (discontinuities) that correspond to large instantaneous-frequency excursions. These phase spikes can cause spectral regrowth and complicate the design of phase-locked loops (PLLs) in the RF chain. In parallel, the envelope path remains vulnerable to high peaks, motivating the use of crest-factor reduction (CFR) techniques to curb PAPR before amplification.

This thesis is motivated by the need to design, model, and evaluate a digital polar-modulation transmitter that mitigates both high PAPR and abrupt phase transitions while meeting the IEEE 802.11a spectral mask (and related quality metrics). The work combines MATLAB simulation with register-transfer-level (RTL) implementation to develop and validate two key baseband blocks: CFR for the envelope path and phase smoothing for the phase path. Their effectiveness is assessed within a complete transmitter chain against standard compliance criteria.

1.2 Problem Definition

While polar modulation offers significant efficiency gains for wireless transmitters, it introduces two fundamental problems that must be addressed to achieve practical and standards-compliant operation.

OFDM signals exhibit a high peak-to-average power ratio (PAPR). To maintain linearity through the power amplifier (PA), the transmitter must operate the PA with significant output back-off, which directly reduces efficiency. If back-off is insufficient, the PA clips or compresses the signal, and the resulting nonlinear distortion produces spectral regrowth and elevated error-vector magnitude (EVM), risking violation of regulatory spectral masks. Hence, a baseband crest-factor reduction (CFR) mechanism is required to suppress peaks while controlling in-band distortion.

The second problem is associated with the phase component of the polar representation. After decomposition into envelope and phase, the instantaneous phase signal often exhibits abrupt discontinuities, particularly near I/Q zero crossings and after interpolation. These discontinuities manifest as instantaneous frequency spikes, which contribute to spectral regrowth and complicate phase-locked loop (PLL) tracking in hardware implementations. A phase-smoothing mechanism is therefore needed to limit large, wrapped deltas while preserving the underlying information.

In addition, polar transmitter architectures are inherently sensitive to mismatches between the envelope and phase paths. Even small delays between the two components can lead to distortion in the reconstructed RF signal, further degrading error vector magnitude (EVM) and spectral containment.

How can a digital polar transmitter for OFDM signals be designed to mitigate high PAPR in the amplitude path and sharp phase discontinuities in the phase path, while ensuring compliance with IEEE 802.11a requirements and maintaining compatibility with practical hardware implementation?

1.3 Objectives and Scope

This thesis investigates, designs, and validates digital techniques that make polar-modulation transmitters practical for OFDM. The work aims to reduce peak power in the envelope path through crest-factor reduction, suppress wrapped phase discontinuities in the phase path through phase smoothing, preserve latency alignment between the two paths so that polar recombination maintains fidelity, and demonstrate implementability in fixed-point RTL with bit-true agreement to a MATLAB reference.

The scope spans algorithmic modelling and hardware-oriented validation. In MATLAB, an end-to-end chain is constructed comprising sample generation, IFFT, interpolation, Cartesian-to-polar conversion, crest-factor reduction, phase smoothing, polar recombination, and performance assessment. Evaluation considers peak-to-average power ratio, error vector magnitude, and out-of-band emissions with respect to the IEEE 802.11a spectral mask. In implementation, the key baseband blocks—a CORDIC for Cartesian-to-polar conversion, a crest-factor reduction module for the envelope path, and a phase-smoothing unit for the phase path are realised in Verilog RTL. Their fixed-point behaviour is verified to be bit-true with respect to the MATLAB models, and synthesis is used to gauge timing and resource feasibility.

Analog and RF design aspects (including power amplifiers and phase-locked loops), complete digital predistortion design, antenna and front-end considerations, channel coding and MAC-layer issues, and over-the-air measurement are not treated. The focus remains on digital baseband algorithms and their implementability; nevertheless, the results are directly relevant to polar transmitter architectures that target efficiency and spectral compliance.

2 CHAPTER 2: Literature Review and Theoretical Background

2.1 Quadrature Amplitude Modulation (QAM)

Quadrature Amplitude Modulation (QAM) conveys information by modulating the in-phase I(t) and quadrature Q(t) components of a carrier simultaneously, placing each symbol at a point in a two-dimensional constellation [1]. For a passband representation with carrier f_c .

$$s(t) = I(t)\cos(2\pi f_c t) - Q(t)\sin(2\pi f_c t)$$

which is equivalent to the complex-baseband form

$$s(t) = \Re\{ (I(t) + jQ(t))e^{j2\pi f_c t} \}$$

In digital baseband systems, incoming bits are grouped and mapped (typically with Gray Coding) to constellation points; the de-mapper performs the inverse operation. An M-QAM constellation contains M points and carries $\log_2 M$ bits per symbol, trading data rate against noise robustness.

Square (rectangular) QAM constellations are most common in practice because they offer separable PAM levels on the I and Q axes and efficient de-mapping. For example, 16-QAM uses four amplitude levels per axis, encodes four bits per symbol, once normalized, exhibits higher SNR requirements than QPSK for the same target error rate.

In OFDM systems, QAM is typically applied per subcarrier. The IEEE 802.11a PHY employs BPSK, QPSK, 16-QAM, and 64-QAM across its data rates; its standard constellation definitions are square (rectangular) QAM. These constellations are later used for EVM and spectral-mask compliance assessments in this thesis [1][2][3].

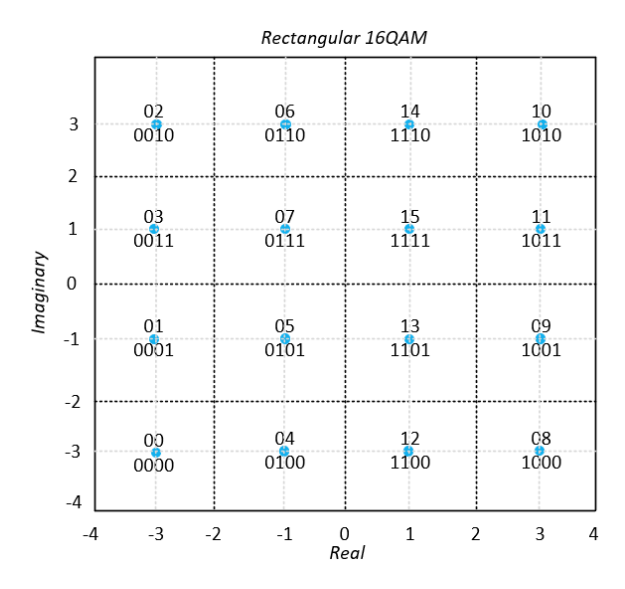


Figure 1: Rectangular 16-QAM constellation with decision regions

2.2 OFDM and IEEE 802.11a Overview

2.2.1 OFDM Principles

Orthogonal Frequency-Division Multiplexing (OFDM) partitions the available bandwidth into many closely spaced orthogonal subcarriers. Each subcarrier carries a low-rate data stream (typically QAM/PSK), so a frequency-selective channel is converted into a set of flat subchannels that are equalized independently at the receiver [4][5].

Let N be the number of subcarriers in one OFDM symbol and s_k the complex data symbol placed on subcarrier k, k = 0,..., N - 1. The time-domain OFDM block produced by the IFFT is the length- N sequence which can be expressed as:

$$x[m] = \frac{1}{N} \sum_{k=0}^{N-1} s_k[n] e^{\frac{j2\pi km}{N}}$$
 , $m = 0,...,N-1$

which is the discrete-time superposition of N complex exponentials. In continuous time, with sampling period T_s and useful symbol duration $T_u = NT_s$, the subcarrier spacing is

$$\Delta f = \frac{1}{T_u}$$

ensuring orthogonality: for $K \neq \ell$

$$\int_0^{T_u} e^{\frac{j2\pi(k-\ell)t}{T_u}} dt = 0$$

This orthogonality permits the individual subcarrier spectra to overlap without inter-carrier interference, maximizing spectral efficiency [4][5].

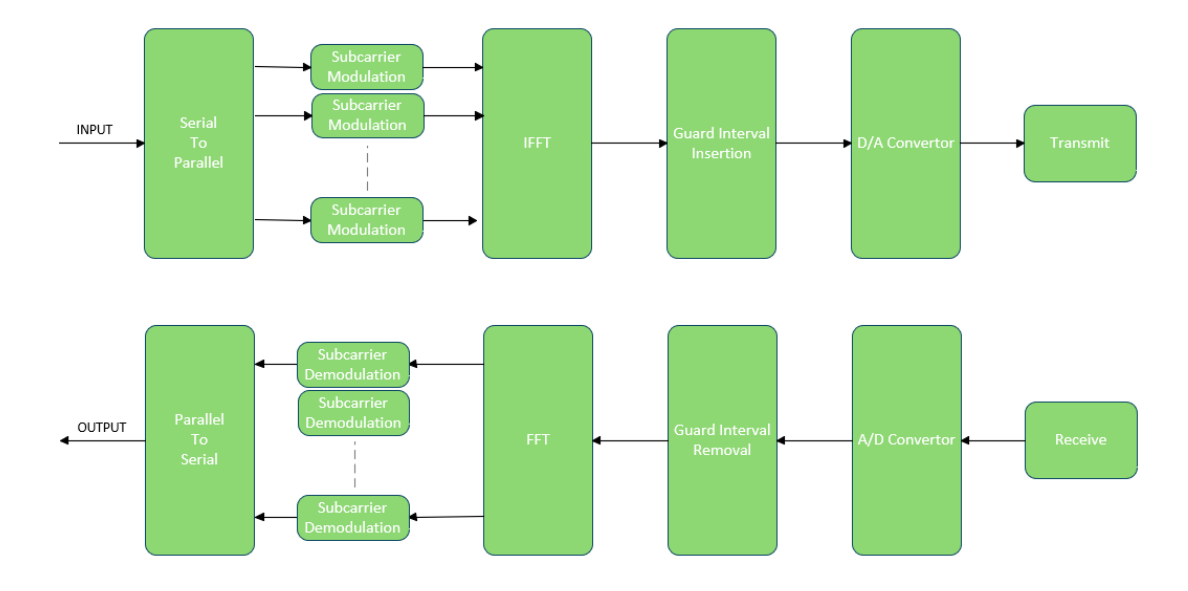


Figure 2:Block diagram of a typical OFDM transmitter and receiver chain, showing IFFT/FFT operations and cyclic prefix addition/removal.

To mitigate inter-symbol interference (ISI) from multipath, a cyclic prefix (CP) is appended; the last N_{CP} samples of x_m are copied to the front. If the CP exceeds the channel's maximum excess delay, the linear channel convolution becomes a circular convolution, so the FFT at the receiver recovers each S[k] with a simple one-tap equalizer per subcarrier. The trade-off is the CP overhead, which slightly reduces data-rate and signal-to-noise ratio [5].

A practical OFDM transmitter therefore maps bits to S[k], applies the IFFT to obtain x_m appends the CP, and converts to the analog domain. The receiver removes the CP, computes the FFT to obtain S[k], equalizes per subcarrier, and demaps the symbols [4][5].

2.2.2 IEEE 802.11a PHY Structure

The IEEE 802.11a standard defines a high-speed physical layer (PHY) operating in the 5 GHz band, designed to provide robust wireless local area network connectivity using orthogonal frequency division multiplexing (OFDM). To ensure reliable transmission in multipath-rich environments, the PHY employs a 64-point Fast Fourier Transform (FFT), with 52 subcarriers actively used: 48 for data transmission and 4 for pilot tones dedicated to phase tracking and frequency offset estimation [4].

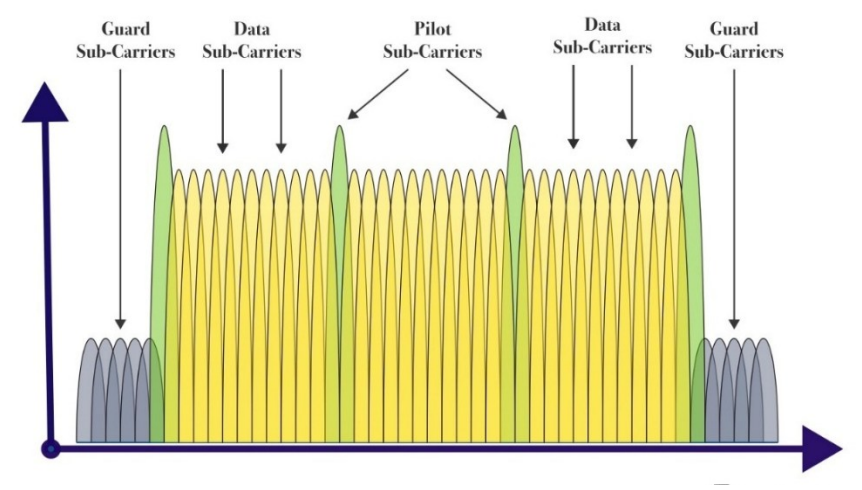


Figure 3: Frequency representation of OFDM symbols

This frequency-domain representation highlights the arrangement of data subcarriers, pilot tones, and guard bands. The overlapping orthogonal spectra of subcarriers maximize spectral efficiency, while guard subcarriers at the band edges mitigate adjacent channel interference.

The subcarrier spacing is 312.5 kHz, resulting in an occupied bandwidth of approximately 16.6 MHz within a nominal 20 MHz channel, allowing guard bands to suppress adjacent channel interference. Supported modulation schemes include BPSK, QPSK, 16-QAM, and 64-QAM, enabling adaptive modulation based on channel conditions to balance throughput and reliability [4].

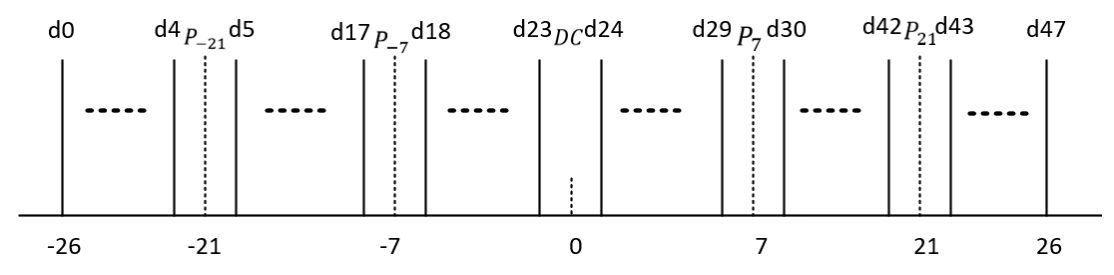


Figure 4:OFDM subcarrier allocation with pilot positions

This diagram (Fig. 4) shows the exact allocation of data and pilot subcarriers within the 64-point FFT grid. Pilot subcarriers, located at fixed indices (-21, -7, +7, +21), play a key role in phase tracking and coherent demodulation, particularly under mobility or oscillator mismatch.

Each OFDM symbol comprises a useful symbol period of 3.2 μ s and a cyclic prefix (guard interval) of 0.8 μ s, extending the total symbol duration to 4 μ s. The cyclic prefix mitigates inter-symbol interference due to multipath delay spread, ensuring correct FFT recovery at the receiver.

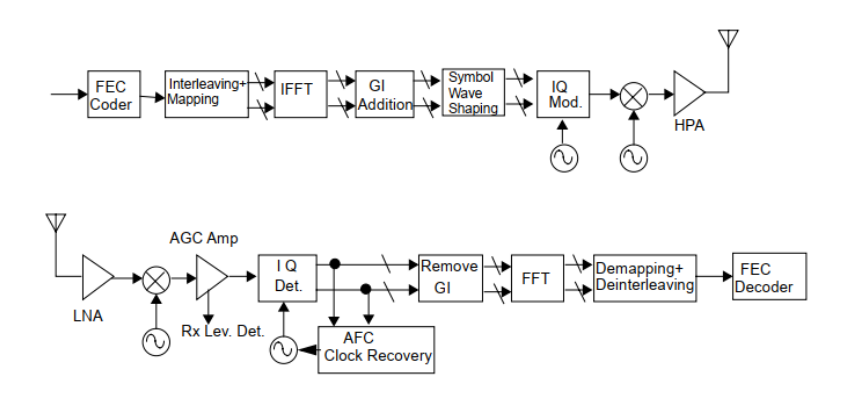


Figure 5: Transmitter and receiver block diagram for the OFDM PHY [4]

The corresponding transmitter and receiver chain includes forward error correction, subcarrier mapping, IFFT/FFT operations, cyclic prefix addition/removal, and pilot-aided synchronization. At the receiver side, frequency and timing recovery circuits ensure robustness against channel and hardware impairments.

The PHY frame structure consists of a Physical Layer Convergence Procedure (PLCP) preamble and header preceding the data payload. The preamble includes a short training sequence for automatic gain control and coarse synchronization, followed by a long training sequence for fine frequency correction and accurate channel estimation.

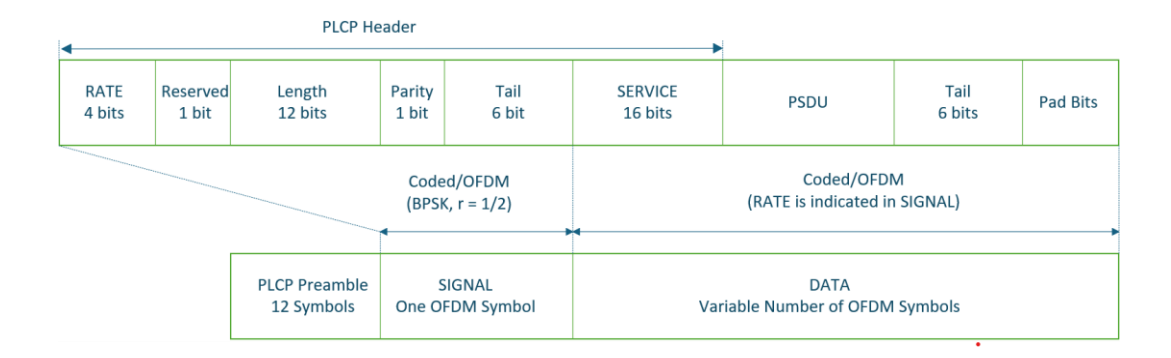


Figure 6: PPDU frame format.

As illustrated in the Fig. 6, the PLCP frame begins with a preamble, followed by a SIGNAL field conveying the transmission parameters, and finally the DATA field containing the coded OFDM symbols.

IEEE 802.11a OFDM PHY Parameters			
Parameters	Value		
FFT size(N)	64		
Total Subcarriers used	52 (48 data + 4 pilots)		
Pilot indices	-21, -7, +7, +21		
Subcarrier spacing	312.5 kHz		
Channel Bandwidth	20 MHz		
Modulation Format	BPSK, QPSK, 16-QAM, 64-QAM		
Useful symbol duration T_{u}	3.2 µs		
Cyclic prefix T_g	0.8 µs		
Total OFDM symbol duration T_{sym}	4 μs		
Occupied Bandwidth	≈ 16.6 MHz		

Table 1: Configuration of the IEEE 802.11a OFDM PHY (FFT=64, 52 used subcarriers)

Table 1 summarizes the most relevant PHY parameters, including FFT size, subcarrier allocation, symbol duration, and supported modulation schemes. These specifications define the basis for evaluating performance in terms of error vector magnitude (EVM) and compliance with spectral masks, as analysed later in this thesis.

2.3 Polar Modulation and CORDIC

2.3.1 Polar Modulation vs. Conventional I/Q Transmitters

Polar modulation represents the transmitted signal in terms of its instantaneous amplitude and phase components, rather than the Cartesian in-phase (I) and quadrature (Q) signals. The baseband signal is decomposed into the envelope A(t) and phase $\emptyset(t)$ and the RF output can be expressed as:

$$S(t) = A(t)\cos(\omega_c t + \emptyset(t))$$

Where ω_c is the carrier angular frequency [6].

This representation allows the RF power amplifier to be driven in a saturated or switching mode since the phase path has constant envelope. As a result, polar transmitters can achieve significantly higher power efficiency compared to conventional I/Q transmitters, which require linear amplification to preserve both the amplitude and phase information carried by the Cartesian signals [6] [7].

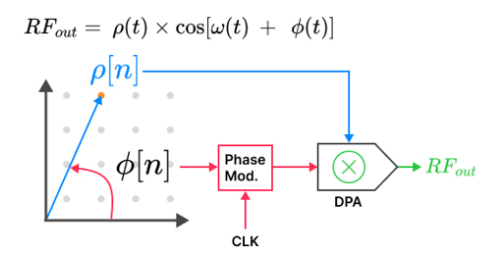
By contrast, conventional I/Q transmitters express the signal as:

$$S(t) = I(t)\cos(\omega_c t) - Q(t)\sin(\omega_c t)$$

and require a linear PA to preserve simultaneous amplitude and phase variations. To avoid nonlinear distortion and spectral regrowth, the PA must be biased with output back-off proportional to the signal's PAPR, which reduces efficiency relative to saturated operation [6][7].

Polar modulation introduces practical challenges. The envelope and phase paths must be precisely time-aligned; even small differential delay produces AM/PM misalignment, degrading EVM and increasing out-of-band emissions. Moreover, the envelope and phase sequences can exhibit bandwidth expansion (e.g., sharp wrapped phase steps and fast envelope dynamics), imposing stricter requirements on the envelope modulator, phase modulator, and their converters. Accurate calibration of gain, delay, and skew between the two paths is therefore essential for spectral compliance [6][7].

Fig. 7 contrasts polar and Cartesian digital transmitter architectures. The polar path includes explicit envelope—phase decomposition and a high-efficiency power amplifier (PA) drive, whereas the Cartesian path operates directly on I and Q through a linear PA. In polar architectures, the switched or digital PA achieves high efficiency but still requires sufficient linearity in its AM/AM (amplitude-to-amplitude) characteristic to avoid distortion. Since multicarrier signals such as OFDM exhibit large envelope peaks, crest factor reduction is applied also in polar transmitters to maintain spectral compliance and modulation accuracy. The illustration therefore highlights both the structural differences and the motivation for polar modulation in power-efficient yet linear transmitter design [6].



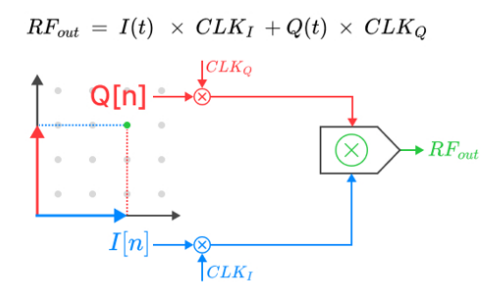


Figure 7: Comparison of polar and Cartesian digital transmitter architectures

2.3.2 Envelope and Phase Separation

In digital polar transmitter architectures, the complex baseband signal must be decomposed into amplitude (envelope) and angle (phase) components to enable separate processing paths for amplitude and phase modulation. This decomposition allows the transmitter to employ highly efficient, nonlinear RF power amplifiers for the envelope path while still preserving accurate overall signal reconstruction through the phase path [8][9].

Mathematically, each baseband sample x[n] can be transformed into polar form by computing its envelope as:

$$|x[n]| = \sqrt{I[n]^2 + Q[n]^2}$$

and its instantaneous phase as:

$$\varphi = \tan^{-1}\left(\frac{Q[n]}{I[n]}\right)$$

This transformation is typically implemented using the Coordinate Rotation Digital Computer (CORDIC) algorithm, which efficiently performs iterative vector rotations in the digital domain [14][16]. The separated phase component is processed by a phase modulator, while the envelope component controls the supply or bias of the power amplifier, ensuring accurate signal reproduction with high efficiency and compliance with linearity requirements [8][9].

2.3.3 CORDIC Algorithm

The Coordinate Rotation Digital Computer (CORDIC) algorithm is an iterative computational method that performs trigonometric, hyperbolic, and linear functions using only addition, subtraction, bit-shifting, and table lookups. This property makes it highly attractive for fixed-point and low-power hardware implementations [11].

CORDIC operates in two main modes, rotation mode and vectoring mode. In rotation mode, a vector is rotated by a sequence of predefined micro-rotations until it reaches a target angle. In contrast, in vectoring mode, which is the one relevant for Cartesian-to-polar conversion, the algorithm progressively aligns an input vector (x, y) with the x-axis by driving its y-component toward zero. During this process, the final x-component gives the magnitude, while the accumulated microrotation angle represents the phase of the original vector [11].

The iterative update equations for the circular (trigonometric) case are expressed as:

$$\begin{cases} x_{i+1} = x_i - m \cdot d_i \cdot 2^{-i} y_i \\ y_{i+1} = y_i + d_i \cdot 2^{-i} x_i \\ z_{i+1} = z_i - d_i \cdot \alpha_i \end{cases}$$

where d_i is the rotation direction, $\alpha_i = \arctan 2^{-i}$ is the predefined micro-rotation angle, and m indicates the coordinate system (+1 for circular, -1 for hyperbolic) [11]. Due to the scale factor introduced by these microrotations, the output must be adjusted by the constant:

$$K = \prod_{i=0}^{n-1} \frac{1}{\sqrt{1 + 2^{-2i}}}$$

which converges as the number of iterations n increases [11].

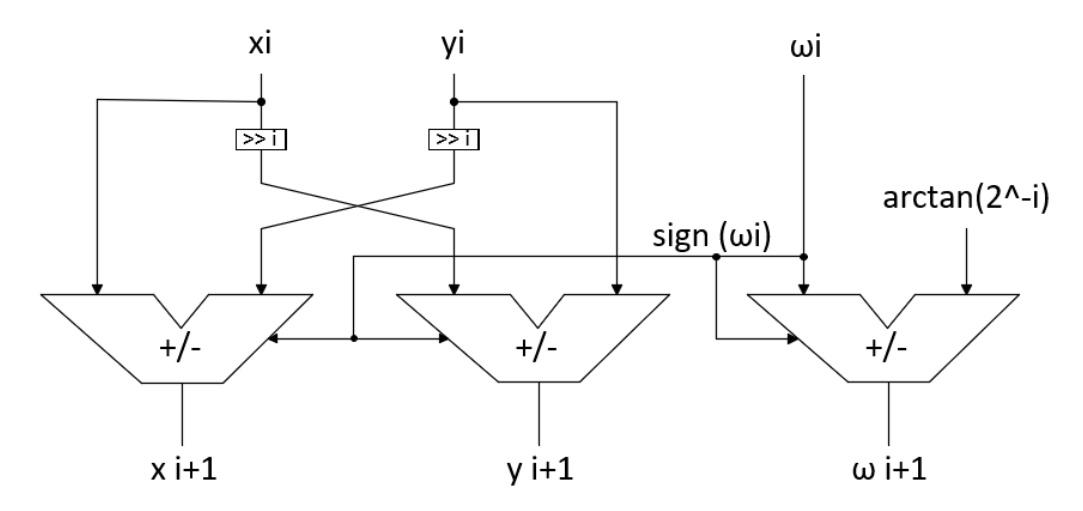


Figure 8: Block diagram of a basic CORDIC iteration cell

A hardware view of one CORDIC iteration is shown in *Fig.* 8, where each stage requires only shift-and-add operations, making the algorithm highly efficient for VLSI implementations.

2.3.4 Application of CORDIC in OFDM & PAPR

In practical OFDM systems, the CORDIC algorithm is widely integrated to perform envelope and phase extraction, frequency offset estimation, and peak detection tasks with high efficiency and minimal hardware cost. For example, in [12], a low-power and high-speed CORDIC architecture is embedded within an autocorrelator to estimate carrier frequency offset (CFO) and aid synchronization in OFDM receivers. This implementation avoids multipliers by relying on shift-add operations, while accurately computing vector magnitude and phase for coarse CFO correction and channel estimation.

Similarly, as demonstrated in [13], CORDIC modules are employed in peak cancellation circuits for real-time PAPR reduction. Here, a pipelined CORDIC core converts incoming complex OFDM samples into amplitude and phase, enabling the system to detect and suppress peaks that exceed a set threshold. The design balances fixed-point word length and hardware cost to maintain low latency and high throughput, fulfilling the tight timing constraints of the OFDM feedback loop

These hardware-oriented designs illustrate how CORDIC supports efficient vector rotations, precise magnitude-phase separation, and dynamic peak control in OFDM transmitters and receivers, thereby enhancing spectral containment and system robustness.

3 Chapter3: Problem Definition & Analysis

3.1 PAPR in OFDM

3.1.1 Mathematical Definition of PAPR

In orthogonal frequency division multiplexing (OFDM) systems, the peak-to-average power ratio (PAPR) quantifies the ratio between the maximum instantaneous power and the average power of a transmitted signal over one symbol duration. This metric is significant because a high PAPR requires power amplifiers to operate within a wide linear region, which reduces power efficiency.

Let x[m] denote the complex, discrete-time OFDM waveform for one symbol (length N), typically after oversampling to capture peaks. The PAPR is [14][15]:

$$PAPR = \frac{\max |x[m]|^{2}_{0 \le m < N}}{\frac{1}{N} \sum_{m=0}^{N-1} |x[m]|^{2}} = \frac{\max |x[m]|^{2}_{0 \le m < N}}{E[|x_{n}|^{2}]}$$

where $|x_n|^2$ represents the instantaneous power and $E[|x_n|^2]$ denotes the average signal power across the entire OFDM symbol. The numerator captures the largest power peak, while the denominator provides the mean power level, making the PAPR a key parameter in evaluating the efficiency and linearity requirements of OFDM transmission systems [15].

3.1.2 Origin of High PAPR in Multicarrier Systems

The High PAPR in OFDM originates from the constructive superposition of multiple independently modulated subcarriers. When these subcarriers, each represented by a complex sinusoid, align constructively in phase at certain instants, they produce signal peaks significantly larger than the average power level [16][17]. Mathematically, this constructive interference is a direct consequence of summing a large number of random-phase carriers, which can occasionally combine coherently, generating unusually high amplitude samples [16].

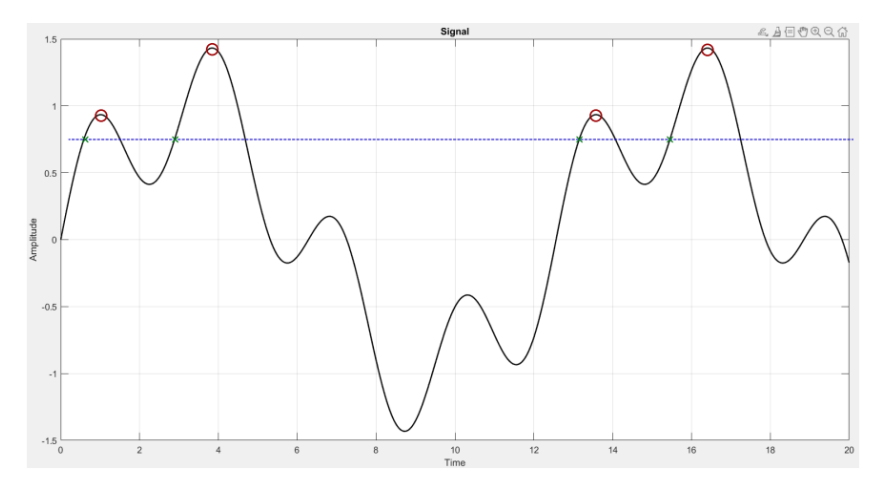


Figure 9: Example waveform envelope showing peaks due to in-phase subcarrier addition.

From a statistical perspective, the time-domain OFDM signal; formed by applying an inverse discrete Fourier transform (IDFT) to modulated symbols behaves like a Gaussian process as the number of subcarriers increases due to the central limit theorem [16][18]. This Gaussian-like behaviour implies that the probability of large amplitude peaks increases with the number of subcarriers, which in turn raises the PAPR. Consequently, OFDM systems with more subcarriers tend to exhibit larger peak-to-average power ratios compared to single-carrier systems [15][17].

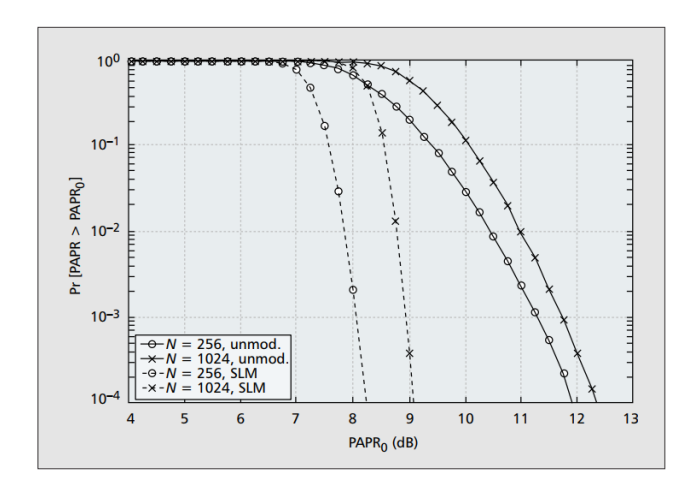


Figure 10: CCDFs of PAPR of an OFDM signal with 256 and 1024 subcarriers for QPSK modulation and oversampling factor 4

3.1.3 Impact on Power Amplifiers

A high peak-to-average power ratio (PAPR) poses significant challenges for power amplifiers (PAs) in multicarrier systems such as OFDM. Because the signal envelope varies widely, a PA must operate with considerable output back-off from its saturation point to maintain linearity and avoid signal distortion [18][19]. This back-off prevents the amplifier from entering its nonlinear region when handling occasional high peaks, but it also reduces the amplifier's power efficiency, leading to increased power consumption and heat generation [18][19].

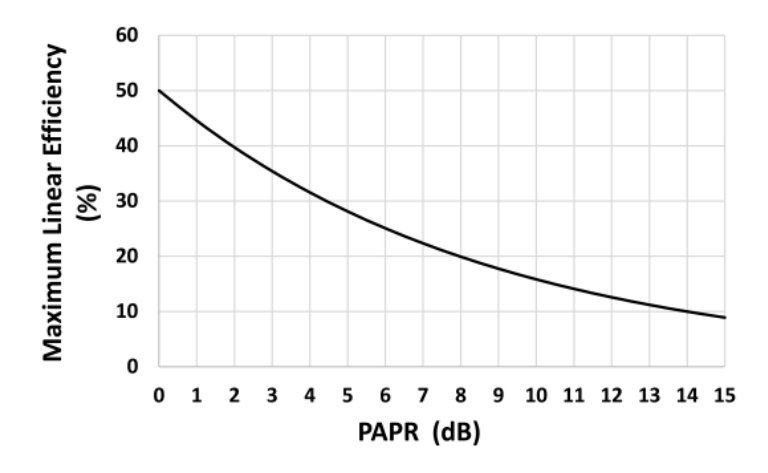


Figure 11: Power amplifier efficiency declines with increasing output back-off [19].

When the back-off is insufficient, the amplifier is driven into its nonlinear region during peak excursions. This nonlinearity produces both in-band distortion which degrading modulation accuracy and out-of-band distortion that cause spectral regrowth. Moreover, results in violations of regulatory emission masks, which strictly limit adjacent-channel leakage. Consequently, high PAPR not only lowers efficiency but also threatens compliance with spectral requirements, underscoring the need for effective PAPR reduction techniques. [15][18].

3.2 Phase Discontinuities and Instantaneous Frequency Spikes

3.2.1 Instantaneous Frequency Spikes

Abrupt phase transitions between consecutive samples—especially when the I/Q trajectory passes near the origin—produce large instantaneous-frequency spike. For a complex envelope:

$$x(t) = r(t)e^{j\emptyset(t)},$$

the instantaneous frequency relative to the carrier is:

$$f_{inst}(t) = \frac{1}{2\pi} \cdot \frac{d\emptyset(t)}{dt}$$

When the phase changes sharply, particularly near points where the I/Q trajectory crosses close to the origin in the polar domain, the derivative $\frac{d\phi(t)}{dt}$ becomes large, generating short-term frequency excursions [21][22]. This behaviour is illustrated in Fig. 12; when the signal has a large amplitude, the phase difference $\Delta \phi_1$ 1 between consecutive samples is relatively small, leading to smooth phase evolution. In contrast, when the trajectory passes close to the origin, the same vector rotation results in a much larger $\Delta \phi_2$. In extreme cases, crossing exactly through the origin can produce abrupt jumps approaching π radians, which manifest as instantaneous frequency spikes.

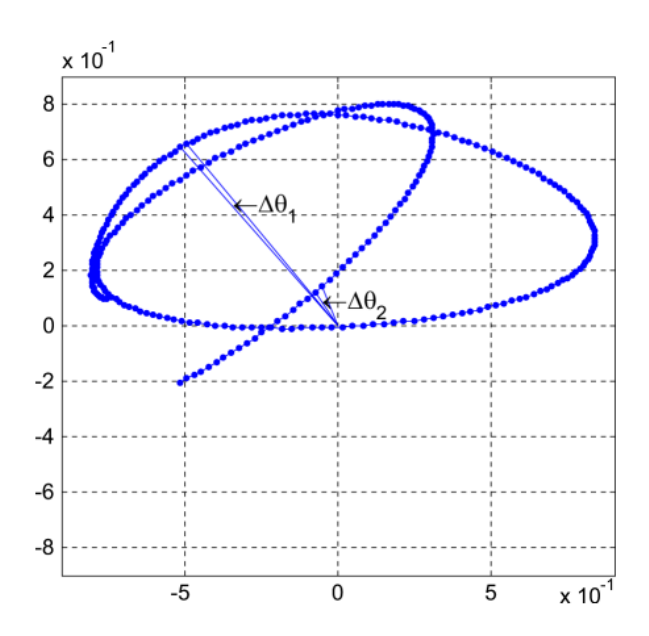


Figure 12: Example of large instantaneous frequency deviation due to phase jumps [21]

In digital polar transmitters, the baseband I/Q signal is converted to amplitude and phase by a CORDIC block; any sudden trajectory near-zero crossings can trigger these large phase jumps, resulting in frequency spikes [21][22]. Such spikes can degrade spectral purity, cause spectral regrowth, and potentially violate emission constraints specified by standards such as IEEE 802.11a [20].

3.2.2 Impact on PLL and Spectrum

In polar transmitters, large instantaneous frequency excursions caused by abrupt phase changes place strict constraints on the phase-locked loop (PLL) and its digitally controlled oscillator (DCO). When the baseband phase trajectory crosses near the origin, the phase increment between consecutive samples can become very large, translating into wide frequency deviations (Δf).

The main design challenge is the tuning range that the DCO must support. Wide Δf excursions require the DCO to span a large frequency range, which increases circuit complexity, reduces efficiency, and worsens phase noise. Typical silicon DCOs offer only limited frequency agility, so forcing them to cover unnecessarily large swings is impractical. While the DPLL maintains lock, its performance is strongly affected because the DCO must respond to large modulation steps within its control range. [22].

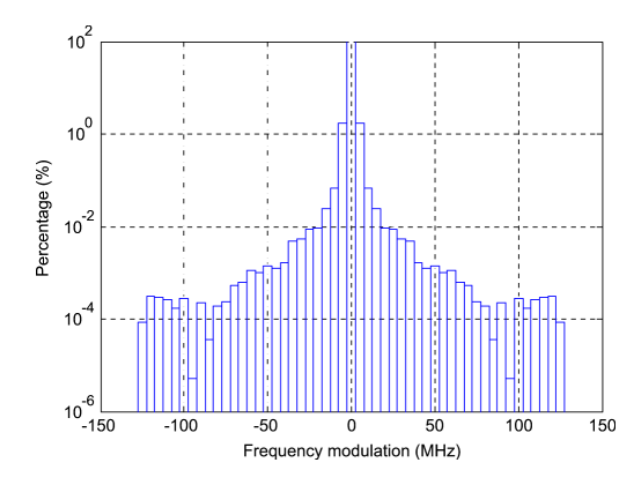


Figure 13: Probability distribution of sample frequency modulation at the 245.76 Mhz CORDIC output in a WCDMA polar modulator [22]

At the same time, widening the PLL loop bandwidth to better track fast variations comes at the cost of increased close-in phase noise, degrading spectral purity [22]. If abrupt excursions are left uncontrolled, the resulting spectral regrowth produces adjacent-channel leakage and can violate emission masks such as those mandated by IEEE 802.11a [23].

To mitigate these issues, phase trajectory smoothing is introduced at the digital baseband. By redistributing large phase jumps across neighbouring samples, the required Δf range is reduced to stay within the DCO's practical tuning capability. This not only relaxes oscillator design constraints but also improves spectral containment and ensures compliance with emission masks [22].

4 CHAPTER 4: Predistortion Techniques for Digital Polar Modulators

High peak-to-average power ratio (PAPR) in the amplitude path and sharp phase discontinuities in the phase path represent two major impairments of digital polar transmitters. If left unmitigated, these effects lead to spectral regrowth, reduced power efficiency, and instability in practical hardware implementations. To overcome these limitations, this work employs digital predistortion techniques applied directly to the separated envelope and phase signals, ensuring both spectral compliance and hardware feasibility.

Two complementary strategies are introduced:

• Amplitude Clipping

This method reduces the PAPR by directly truncating signal peaks that exceed a predefined threshold. Its implementation is straightforward and highly effective in lowering peak levels. However, clipping introduces both in-band distortion, which degrades modulation accuracy, and out-of-band spectral regrowth, which may compromise compliance with spectral masks.

• Window-Based Crest Factor Reduction (Peak Windowing)

Applied to the amplitude sequence, CFR lowers the PAPR by attenuating peaks above a defined threshold and redistributing the excess energy using a Hamming-window-based correction. This method reduces out-of-band radiation while maintaining an acceptable level of in-band distortion.

• Phase Smoothing

Applied to the phase trajectory, this method redistributes abrupt discontinuities across neighbouring samples. By limiting instantaneous phase jumps, it suppresses frequency spikes that would otherwise impair spectral containment and degrade phase-locked loop (PLL) tracking.

These three techniques form the core of the predistortion framework for digital polar modulation. The following sections detail their design, implementation, and evaluation.

4.1 PAPR Reduction Methods

4.1.1 Amplitude Clipping

Amplitude clipping is one of the most straightforward signal distortion techniques employed to reduce the peak-to-average power ratio (PAPR) in orthogonal frequency-division multiplexing (OFDM) systems. In this approach, the amplitude of the OFDM signal is limited to a predefined threshold; when the instantaneous amplitude exceeds this level, it is clipped to the maximum allowed value while its phase remains unchanged (Fig. 14) [24].

The main advantage of simple clipping is its simplicity and very low computational cost, making it suitable for real-time systems [15]. However, this method introduces in-band distortion that degrades modulation accuracy (EVM) and generates out-of-band radiation, which can interfere with adjacent channels and compromise spectral efficiency. Although filtering is commonly applied to suppress out-of-band emissions, this can lead to peak regrowth, necessitating repeated clipping and filtering operations to maintain the desired amplitude constraint [24][15].

4.1.2 Window-Based Crest Factor Reduction (Peak Windowing)

Window-based crest factor reduction, also known as peak windowing, is an effective signal conditioning technique for reducing the peak-to-average power ratio (PAPR) in multicarrier systems such as OFDM. In this method, signal samples that exceed a specified amplitude threshold are selectively attenuated by applying a finite-length window function, such as Hanning, Kaiser, or Raised Cosine, which smooths the peak and redistributes its energy across adjacent samples [15][25].

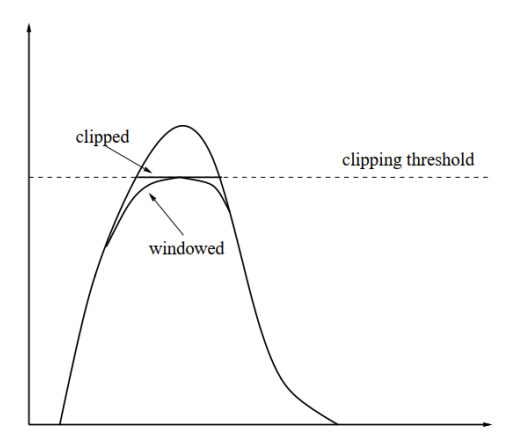


Figure 14: Clipped signal vs. windowed signal 1251

This targeted smoothing reduces the abrupt transitions caused by hard clipping and consequently lowers out-of-band radiation, improving spectral containment [25].

The windowing operation can be mathematically expressed as follows:

$$y[n] = x[n] - \sum_{k=-M}^{M} w[k].p[n-k]$$

where x[n] denotes the original signal, p[n] represents the detected peak impulse, w[k] is the window function, and the sum runs over a finite range $-M \le k \le M$ [10].

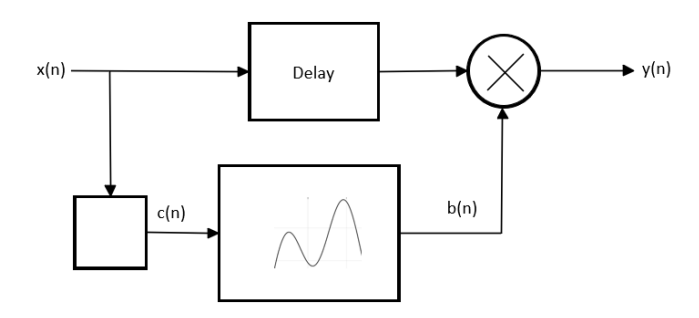


Figure 15: Block diagram of windowing method

Unlike simple amplitude clipping, peak windowing subtracts a window-shaped correction that redistributes the excess amplitude over neighbouring samples. This smoother treatment reduces out-of-band spectral regrowth and improves compliance with the spectrum mask; however, because the correction perturbs the in-band constellation more persistently, its EVM is typically worse than clipping at the same threshold. Conversely, clipping concentrates most of the distortion out of band, so it achieves better modulation accuracy (lower EVM) but exhibits poorer spectral containment.

4.2 Window Functions for Peak Smoothing

4.2.1 Hamming Window Theory

The Hamming window is a widely used time-domain weighting function that plays a crucial role in window-based crest factor reduction for multicarrier systems such as OFDM. Its primary purpose is to taper the amplitude of signal samples in the vicinity of detected peaks, thereby ensuring a smooth transition and suppressing sharp discontinuities that would otherwise produce undesirable spectral leakage [25][26]. By applying this window to large signal excursions, the system can effectively limit out-of-band radiation while maintaining good spectral efficiency and moderate computational complexity.

Mathematically, the Hamming window of length N is defined by the standard raised cosine formula:

$$w(n) = 0.54 - 0.46 \cos\left(\frac{2\pi n}{N-1}\right), \qquad 0 \le n \le N-1$$

This weighting profile offers a narrow main lobe with significantly reduced side lobe levels, striking a balance between time-domain smoothing and frequency-domain containment [25][26]. When integrated into peak windowing algorithms, the Hamming window minimizes abrupt amplitude changes around high peaks, thereby lowering the peak-to-average power ratio (PAPR) without introducing excessive in-band distortion [25].

4.2.2 FIR Filter Design

Finite Impulse Response (FIR) filters are a fundamental component in mitigating the spectral regrowth that occurs when signal peaks are suppressed by methods such as clipping or peak windowing in OFDM systems. When the time-domain signal is clipped to limit its amplitude, high-frequency components are inevitably generated, which can cause the transmitted signal to violate regulatory spectral masks and produce adjacent channel interference [27][28]. To counteract this, an FIR filter is designed to selectively remove these unwanted out-of-band frequencies while preserving the integrity of the desired signal.

A typical low-pass FIR filter used for this purpose is constructed using a windowed sinc function, which defines the filter's impulse response h[n] as:

$$h[n] = w[n]. sinc(2f_c\left(n - \frac{M}{2}\right))$$

where w[n] denotes the chosen window function (e.g., Hamming or Hann), f_c is the normalized cutoff frequency, and M represents the filter order [27]. The use of windowing controls side-lobe behavior, enabling a balance between sharp spectral roll-off and acceptable in-band distortion.

While increasing the filter length improves suppression of out-of-band emissions, it also increases computational complexity and group delay. Therefore, the design process must balance spectral containment, distortion performance, and implementation cost [27][28].

4.3 Phase Smoothing Algorithm

In polar transmitters used for OFDM systems, the conversion from Cartesian to polar coordinates introduces discontinuities in the phase domain. This issue becomes particularly prominent after interpolation stages, where the discrete phase sequence may experience abrupt jumps between adjacent samples. Such discontinuities, typically referred to as phase spikes or sharp $\Delta \varphi$ transitions, result in increased spectral bandwidth and hinder the performance of phase-locked loops (PLLs) in the transmitter chain [21].

To mitigate these effects, a dedicated phase smoothing technique is employed, wherein each sample is monitored for large inter-sample phase differences. If a phase jump exceeds a predefined threshold, a redistribution mechanism is triggered. Specifically, the algorithm uses a 3-point local buffer centered on the current sample. When a spike is detected, the excess phase value is partially redistributed to the previous and subsequent samples, thereby reducing the instantaneous transition and maintaining continuity across the time axis. This localized redistribution reduces the phase derivative ($\frac{d\varphi}{dt}$), thereby suppressing spectral regrowth and improving PLL stability [21][22].

Mathematically, the spike detection relies on computing the discrete difference:

$$\Delta \emptyset(n) = \emptyset(n) - \emptyset(n-1)$$

and comparing it against a fixed threshold. If $\Delta \emptyset(n) > \theta$ the sample is considered a spike, and redistribution is applied as follows:

$$\emptyset(n-1) \leftarrow \emptyset(n-1) + \frac{\Delta \emptyset_{excess}}{4}$$

$$\emptyset(n) \leftarrow \emptyset(n-1) - \frac{\Delta \emptyset_{excess}}{2}$$

$$\emptyset(n+1) \leftarrow \emptyset(n+1) + \frac{\Delta \emptyset_{excess}}{4}$$

Where $\Delta \emptyset_{excess} = \Delta \emptyset(n) - \theta$. This method ensures that the total phase is conserved within the correction window while reducing the occurrence of sharp instantaneous transitions [21][22].

5 Chapter 5: MATLAB Simulation Chain

The MATLAB environment was employed to model and validate the complete digital polar transmitter chain for orthogonal frequency-division multiplexing (OFDM). This simulation framework was designed to reproduce the main processing stages of the transmitter, enabling the assessment of proposed predistortion techniques under realistic conditions before their hardware implementation. The results obtained from the simulations were compared against the IEEE 802.11a compliance standards, including spectrum mask and EVM requirements.

5.1 IEEE 802.11a Compliance

The performance of the proposed methods was assessed against the criteria established by the IEEE 802.11a standard, which defines limits for spectral emission, modulation accuracy, and overall signal quality.

5.1.1 Transmit Spectrum Mask

The transmit spectrum mask specifies the maximum allowable out-of-band emissions at given frequency offsets from the channel centre frequency. As shown in Fig. 16, strict limits are imposed at ± 11 MHz, ± 20 MHz, and ± 30 MHz. All MATLAB and RTL results presented in this chapter include PSD evaluations compared to the reference mask, ensuring that the processed signals do not exceed the regulatory limits.

- At ± 11 MHz: power spectral density must be below -20 dBr,
- At ± 20 MHz: below -28 dBr,
- At ± 30 MHz and beyond: below -40 dBr.

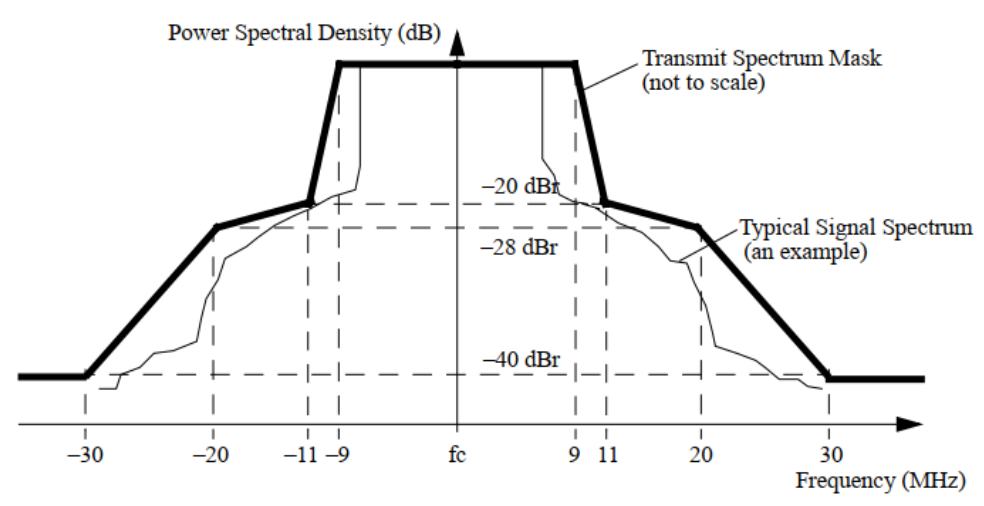


Figure 16: IEEE 802.11a Transmit Spectrum Mask [4].

5.1.2 Modulation Accuracy (EVM)

Error Vector Magnitude (EVM) quantifies the modulation accuracy by measuring the deviation of received constellation points from their ideal positions. According to table 2, the maximum acceptable EVM for 16-QAM at a data rate of 24 Mbps is –16 dB. All methods and configurations presented in this chapter are evaluated with respect to this requirement to ensure compliance.

These limits ensure reliable demodulation and consistent symbol spacing in the presence of noise and distortion. EVM is computed using baseband measurements after carrier recovery, synchronization, and channel correction.

Data Rate (Mbits/s)	Relative constellation Error(dB)
6	-5
9	-8
12	-10
18	-13
24	-16
36	-19
48	-22
54	-25

Table 2: IEEE 802.11a allowed relative constellation error versus data rate [4]

5.2 MATLAB Simulation

The chain begins with 16-QAM symbol generation, followed by subcarrier and pilot mapping, interpolation, and IFFT-based modulation. After guard interval insertion, the Cartesian signal representation is converted into polar form, where crest factor reduction and phase smoothing are applied independently to the amplitude and phase components. The corrected signal is then converted back to Cartesian coordinates for transmission. A simplified receiver chain, including FFT and demodulation, is included to enable error vector magnitude (EVM) evaluation and to provide a consistent performance benchmark.

The overall architecture of the implemented MATLAB simulation chain is shown in Fig. 17. Each block is described in detail in the subsequent sections.

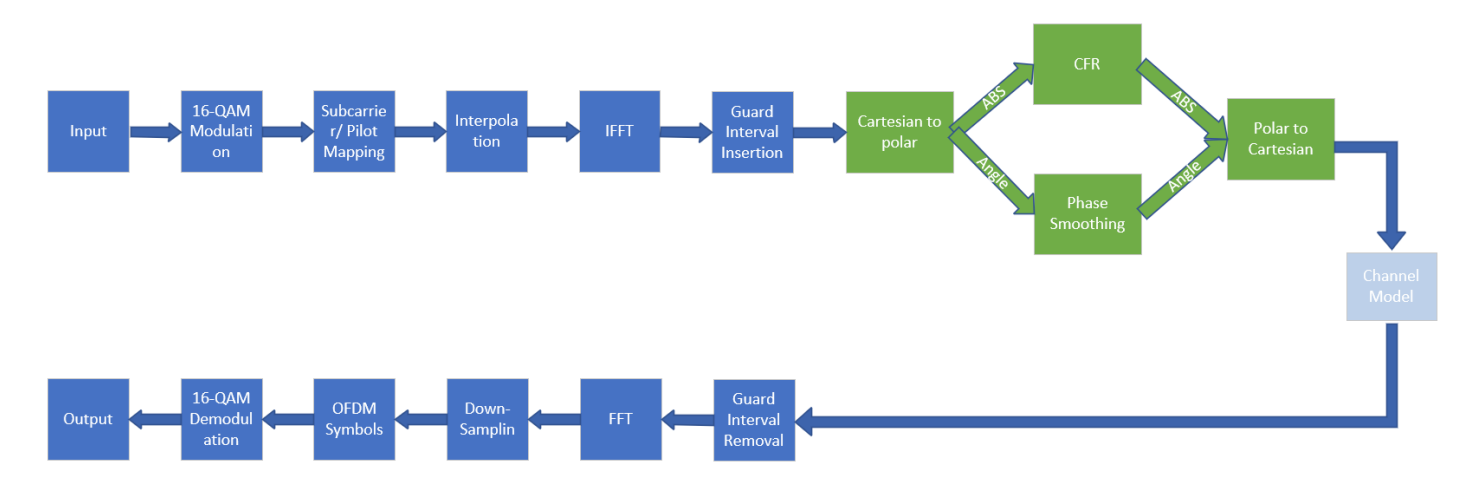


Figure 17:MATLAB simulation chain of the digital polar transmitter

5.2.1 Signal Generation

The MATLAB simulation begins with the generation of random data symbols that are mapped onto a 16-QAM constellation. The constellation is normalized so that the average symbol energy equals unity, thereby ensuring consistent power levels for subsequent processing.

These symbols are then arranged into OFDM frames according to the IEEE 802.11a subcarrier allocation. Each 64-point FFT symbol includes 48 subcarriers reserved for data transmission and 4 pilot subcarriers that provide phase reference and facilitate synchronization. The remaining tones are allocated to guard subcarriers or to the DC null, which suppresses carrier leakage. The detailed allocation scheme is summarized in Table 3.

Subcarrier Index Range	Allocation Type	Count	Description
-32 to -27, +27 to +31	Guard Subcarriers	12	Spectral shaping / no transmission
−26 to −1, +1 to +26	Data Subcarriers	48	Carry QAM-modulated symbols
-21, -7, +7, +21	Pilot Subcarriers	4	Used for phase tracking and synchronization
0	DC (null) Subcarrier	1	Suppresses carrier leakage
Total	FFT Subcarriers	64	Complete OFDM symbol size

Table 3: Subcarrier allocation for 64-point IEEE 802.11a OFDM.

Once mapped, the frequency-domain frame is converted into the time domain using a 64-point inverse fast Fourier transform (IFFT). A cyclic prefix of 16 samples is appended to each OFDM symbol to mitigate inter-symbol interference (ISI). This process produces the baseband OFDM signal, which forms the input to the subsequent interpolation and quantization stages.

5.2.2 Interpolation

Following OFDM symbol mapping and IFFT transformation, interpolation is applied to increase the sampling rate and improve spectral resolution. In this work, interpolation factors of four and eight are supported.

The procedure is implemented in two stages. First, the original time-domain sequence is expanded by zero-insertion, whereby additional zeros are introduced between consecutive samples to achieve the desired up-sampling factor. Second, the up-sampled sequence is passed through a finite impulse response (FIR) interpolation filter, with coefficients predesigned and stored for the selected factor (×4 or ×8). The filtering stage suppresses the spectral images introduced by the zero-insertion process and ensures that the interpolated waveform maintains smooth temporal transitions.

The interpolation process can be formally expressed as:

$$x_{interp}[n] = \sum_{k} x[k].h[n - kL]$$

Where L is the interpolation factor and h[n] is the FIR filter impulse response.

5.2.3 Amplitude Clipping and Peak Windowing

In the MATLAB simulation chain, two peak-reduction strategies were implemented and compared: amplitude clipping and window-based crest factor reduction (CFR). Both methods operate in the amplitude domain after interpolation, while the phase trajectory of the signal remains unaffected.

Amplitude clipping limits the signal magnitude to a fixed threshold. For a given amplitude sequence x[n], the clipped signal $x_{clip}[n]$ is defined as

$$x_{clip}[n] = \begin{cases} T, & x[n] > T \\ x[n], & x[n] \le T \end{cases}$$

where *T* denotes the clipping threshold. This operation effectively reduces the peak-to-average power ratio (PAPR) but introduces in-band distortion that degrades error vector magnitude (EVM) and causes out-of-band radiation.

Window-based crest factor reduction improves upon simple clipping by introducing a smoother peak suppression mechanism. For samples exceeding the threshold, a correction sequence c[n] is generated, representing the amount by which each sample exceeds T. This correction is then shaped by a finite-length window function $\omega[k]$ and redistributed across neighboring samples. The corrected signal is obtained as

$$x_{CFR}[n] = x[n] - (c[n] * \omega[n]),$$

where * denotes convolution. Expanding this relation explicitly gives

$$x_{CFR}[n] = x[n] - \sum_{k=-M}^{M} c[n-k] \omega[k].$$

The use of a Hamming window ensures that energy is smoothly spread across adjacent samples, thereby reducing spectral regrowth while preserving overall signal quality. Both approaches were evaluated in MATLAB in terms of PAPR reduction, EVM degradation, and power spectral density (PSD) compliance with IEEE 802.11a.

Case 1: Threshold = 0.28

Fig. 18 illustrates the power spectral density (PSD) comparison when the amplitude clipping, and peak windowing thresholds are set to 0.28. Both peak-reduction techniques substantially decrease the peak-to-average power ratio (PAPR), reducing it from 11.53 dB in the original signal to 8.26 dB.

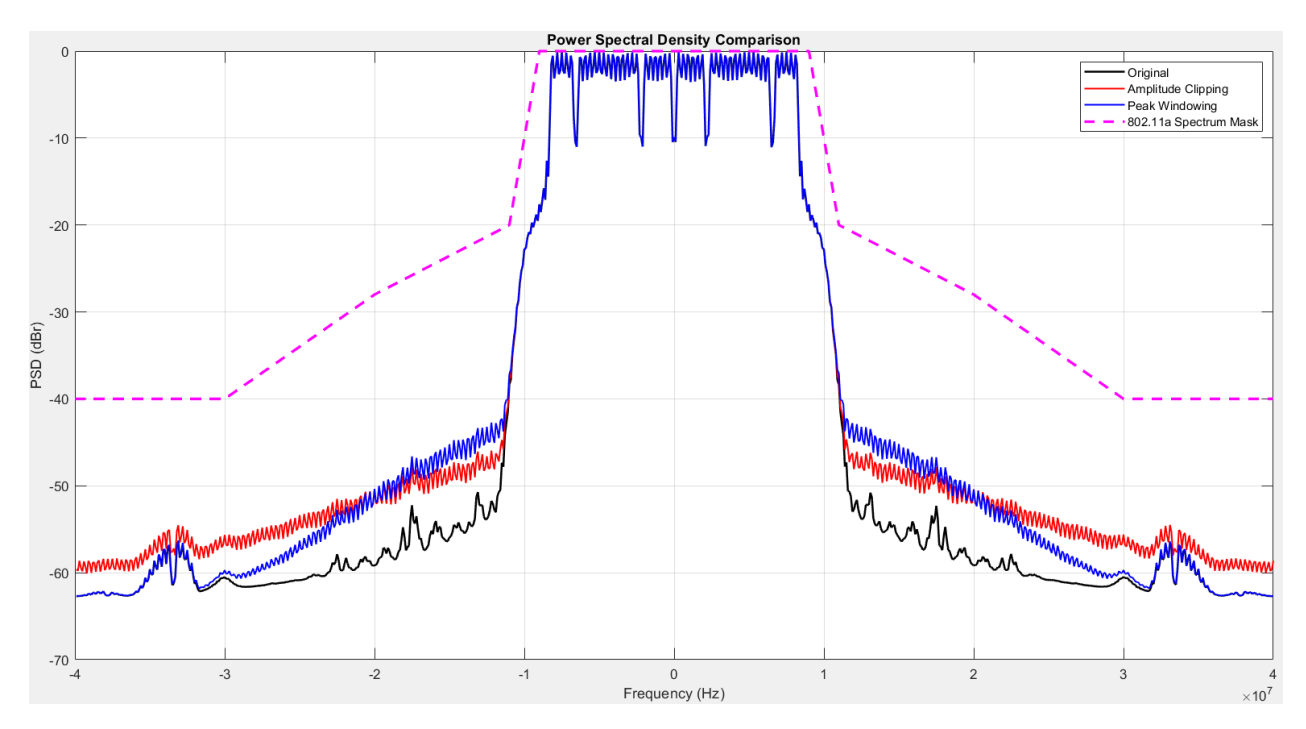


Figure 18:Power spectral density comparison for Clipping and CFR at threshold = 0.28.

Metric	Original Signal	Clipping	P. Windowing
EVM (dB)	-57.48	-45.05	-39.52
PAPR	11.53	8.26	8.26

Table 4

Table 4 summarizes the corresponding error vector magnitude (EVM) and PAPR values. Amplitude clipping achieves better EVM performance (–45.05 dB) compared to peak windowing (–39.52 dB), since part of the distortion energy is shifted into the out-of-band spectrum. On the other hand, peak windowing provides comparable PAPR reduction while applying smoother suppression of peaks.

This behaviour is further confirmed in Table 5, which presents PSD levels at frequency offsets of 11 MHz, 20 MHz, and 30 MHz. Peak windowing demonstrates superior suppression of out-of-band radiation, particularly at 30 MHz, where the PSD is reduced to –59.68 dBr compared to –55.60 dBr for clipping. This improvement highlights its effectiveness in achieving compliance with the IEEE 802.11a spectral mask, even though it introduces slightly higher in-band distortion as reflected in the EVM.

Frequency (MHz)	Original Signal(dBr)	Clipping(dBr)	P. Windowing (dBr)
11	-38.327	-37.802	-37.063
20	-59.138	-50.527	-50.398
30	-60.473	-55.60	-59.684

Table 5

As illustrated, for a threshold of 0.28, both methods effectively reduce PAPR, but clipping yields a lower EVM, while CFR offers better spectral containment and mask compliance.

Case 2: Threshold = 0.22

Fig. 19 presents the power spectral density (PSD) comparison when the clipping and peak windowing threshold is reduced to 0.22. As in the previous case, both techniques significantly lower the PAPR, with values decreasing from 11.46 dB for the original signal to approximately 6.22–6.28 dB.

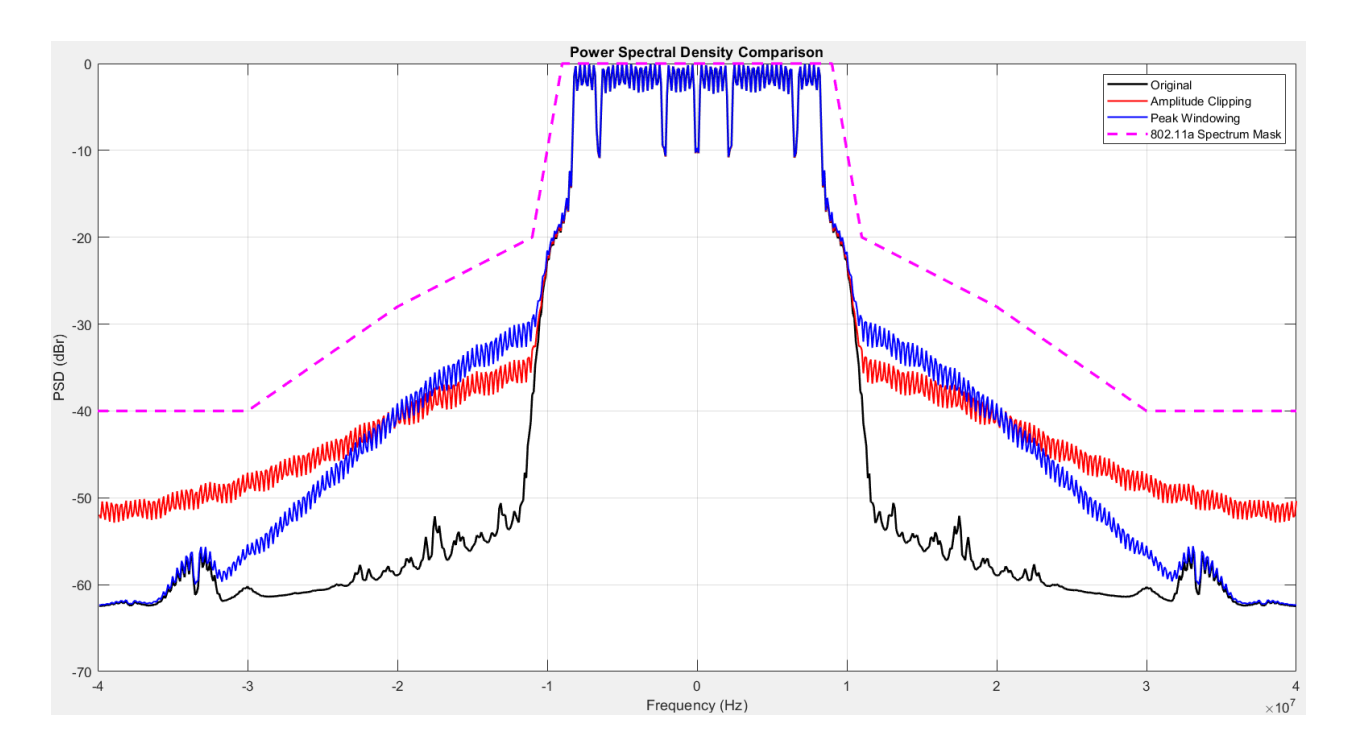


Figure 19: Power spectral density comparison for Clipping and CFR at threshold = 0.22.

Metric	Original Signal	Clipping	P. Windowing
EVM (dB)	-57.44	-31.75	-25.97
PAPR	11.46	6.22	6.28

Table 6

Table 6 summarizes the error vector magnitude (EVM) and PAPR results. At this lower threshold, clipping achieves an EVM of –31.75 dB, while peak windowing results in –25.97 dB. This confirms that clipping continues to provide better in-band signal fidelity, as part of the distortion energy is redistributed outside the useful bandwidth. Peak windowing, on the other hand, preserves similar PAPR performance but shows a more controlled spectral profile.

The difference in spectral containment is highlighted in Table 7, which reports PSD levels at offset frequencies of 11 MHz, 20 MHz, and 30 MHz. Peak windowing achieves stronger suppression of far-out spectral components, particularly at 30 MHz, where the PSD is –55.51 dBr compared to – 47.2 dBr for clipping. This improvement demonstrates that windowing achieves superior compliance with the IEEE 802.11a spectrum mask, even if it introduces higher in-band distortion as reflected in the EVM.

Frequency (MHz)	Original Signal(dBr)	Clipping(dBr)	P. Windowing (dBr)
11	-38.15	-32.981	-29.457
20	-58.922	-39.424	-39.118
30	-60.247	-47.2	-55.514

Table 7

Overall, at a threshold of 0.22, both methods provide effective PAPR reduction. Clipping minimizes EVM degradation, whereas peak windowing offers better out-of-band suppression and improved spectral compliance.

Case 3: Threshold = 0.17

Fig. 20 presents the power spectral density (PSD) comparison for amplitude clipping and peak windowing when the threshold is reduced to 0.17. At this tighter constraint, both methods achieve substantial peak-to-average power ratio (PAPR) reduction, lowering it from 11.96 dB in the original signal to 4.30 dB for clipping and 4.60 dB for peak windowing.

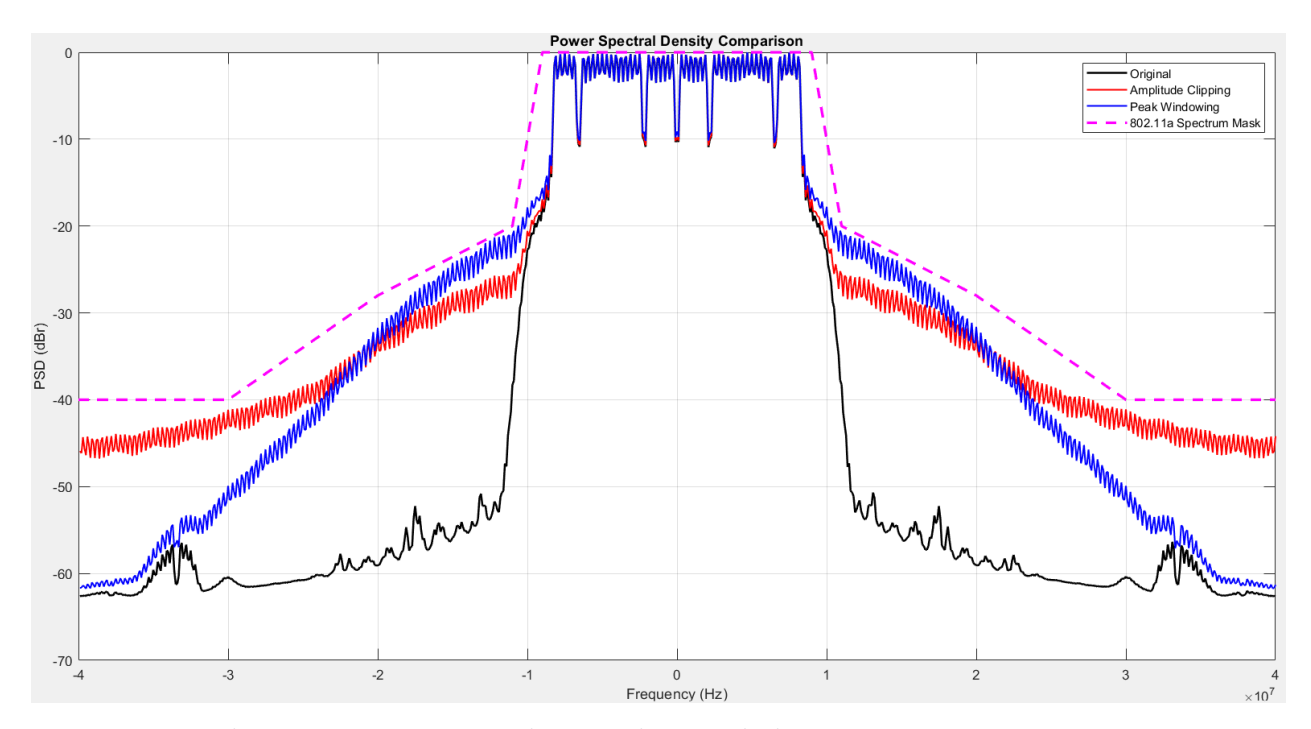


Figure 20:Power spectral density comparison for Clipping and CFR at threshold = 0.17.

Metric	Original Signal	Clipping	P. Windowing
EVM (dB)	-57.40	-22.65	-16.52
PAPR	11.96	4.30	4.60

Table 8

As shown in Table 8, the improvement in PAPR comes at the expense of error vector magnitude (EVM). Clipping reaches –22.65 dB, while peak windowing shows slightly higher degradation at –16.52 dB. The increased EVM is a direct result of stronger non-linear distortion introduced at such a low threshold.

Frequency (MHz)	Original Signal(dBr)	Clipping(dBr)	P. Windowing (dBr)
11	-38.257	-25.651	-21.028
20	-59.041	-32.358	-31.593
30	-60.364	-41.097	-49.906

Table 9

Table 9 confirms the trade-off in the frequency domain. While both methods exhibit higher out-of-band radiation compared to higher thresholds, peak windowing continues to provide better suppression of far-out spectral components. At 30 MHz, for instance, the PSD level for peak windowing (–41.097dBr) is significantly lower than that of clipping (–49.906 dBr).

Overall, at a threshold of 0.17, both techniques effectively reduce PAPR, but the aggressive amplitude constraint leads to more severe in-band distortion. Clipping offers a modest advantage in EVM, while peak windowing ensures superior spectral containment and closer compliance with the IEEE 802.11a mask.

5.2.4 Phase Smoothing

In polar transmitter architectures, the conversion from Cartesian to polar coordinates often introduces abrupt discontinuities in the phase trajectory. These sharp phase jumps $(\Delta\emptyset)$ typically appear near I/Q zero crossings and after interpolation, manifesting as instantaneous frequency spikes. In the frequency domain, such abrupt transitions correspond to the introduction of high-frequency components, which spread energy beyond the allocated band. This phenomenon, known as spectral regrowth, increases adjacent-channel interference and may cause the transmitted signal to violate regulatory spectral masks such as those specified in IEEE 802.11a. Moreover, the presence of spikes can degrade the robustness of phase-locked loops (PLLs), potentially leading to instability in practical hardware.

To address these issues, a phase smoothing algorithm was implemented in MATLAB. The method operates directly in the float domain, where the instantaneous phase sequence is first computed and wrapped to the interval $(-\pi, \pi]$. The difference between successive phase samples $(\Delta\emptyset)$ is then evaluated. If the wrapped difference exceeds a predefined threshold, the excess portion of the phase jump is redistributed across three consecutive samples.

The redistribution follows a fixed ratio: half of the excess is subtracted from the current sample, while one quarter is added to each of the immediate neighbours. This ensures that the overall trajectory becomes smoother, while the total phase across the signal remains preserved. The redistribution process is illustrated in Fig. 21.

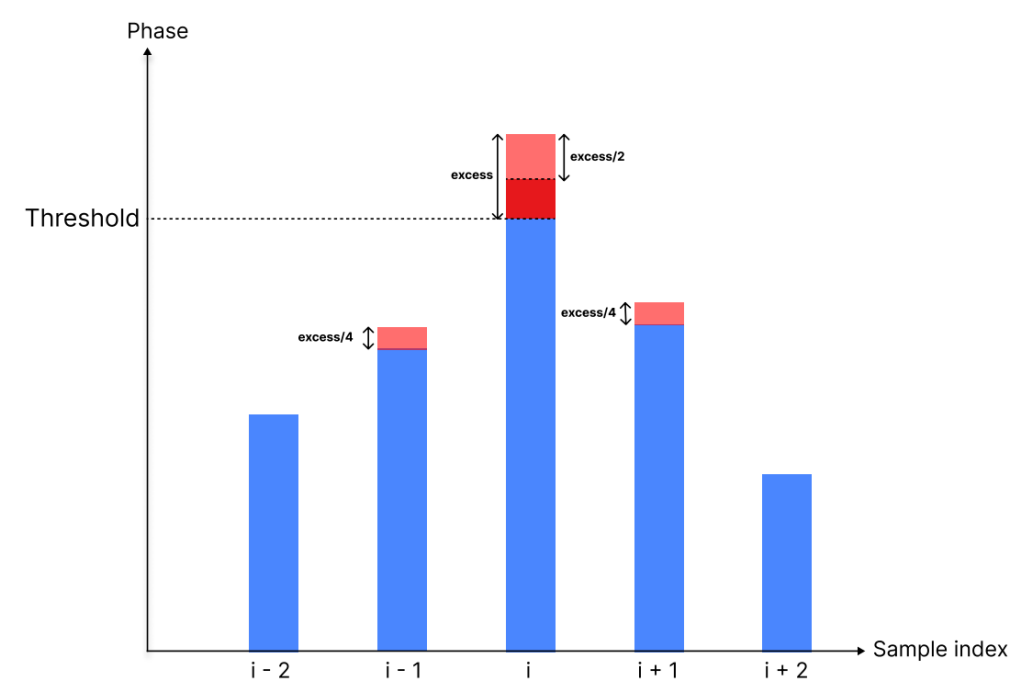


Figure 21: Phase redistribution principle for smoothing algorithm (diagram showing 1/4–1/2–1/4 split).

Mathematically, let

$$\Delta \varphi_{wrapped} = wrap(\emptyset[n] - \emptyset[n-1])$$

denote the wrapped phase difference. If

$$|\Delta \emptyset_{wrapped}| > \emptyset_{th}$$

the correction is applied as:

$$\emptyset(n-1) \leftarrow \emptyset(n-1) + \frac{\Delta \emptyset_{excess}}{4}$$
$$\emptyset(n) \leftarrow \emptyset(n-1) - \frac{\Delta \emptyset_{excess}}{2}$$
$$\emptyset(n+1) \leftarrow \emptyset(n+1) + \frac{\Delta \emptyset_{excess}}{4}$$

where

$$\Delta \emptyset_{excess} = \, \Delta \emptyset_{wrapped} - sign \, (\Delta \emptyset_{wrapped}) \, . \, \emptyset_{th}$$

The result is a smoother phase trajectory that mitigates sudden jumps while preserving total phase continuity. This process effectively reduces frequency-domain sidelobes caused by phase spikes, thereby improving spectral containment without significantly distorting the signal's modulation properties.

Case 1: Threshold = $3\frac{\pi}{4}$

3.32265

3.3227

3.32275

3.3228

Fig. 22 and Fig. 23 illustrate the effect of applying phase smoothing with a threshold of $3\frac{\pi}{4}$ on the instantaneous frequency and power spectral density (PSD). As observed in Fig. 22, the original instantaneous frequency contains abrupt spikes caused by large, wrapped phase differences, while the smoothed version eliminates these discontinuities, resulting in a more stable frequency trajectory.

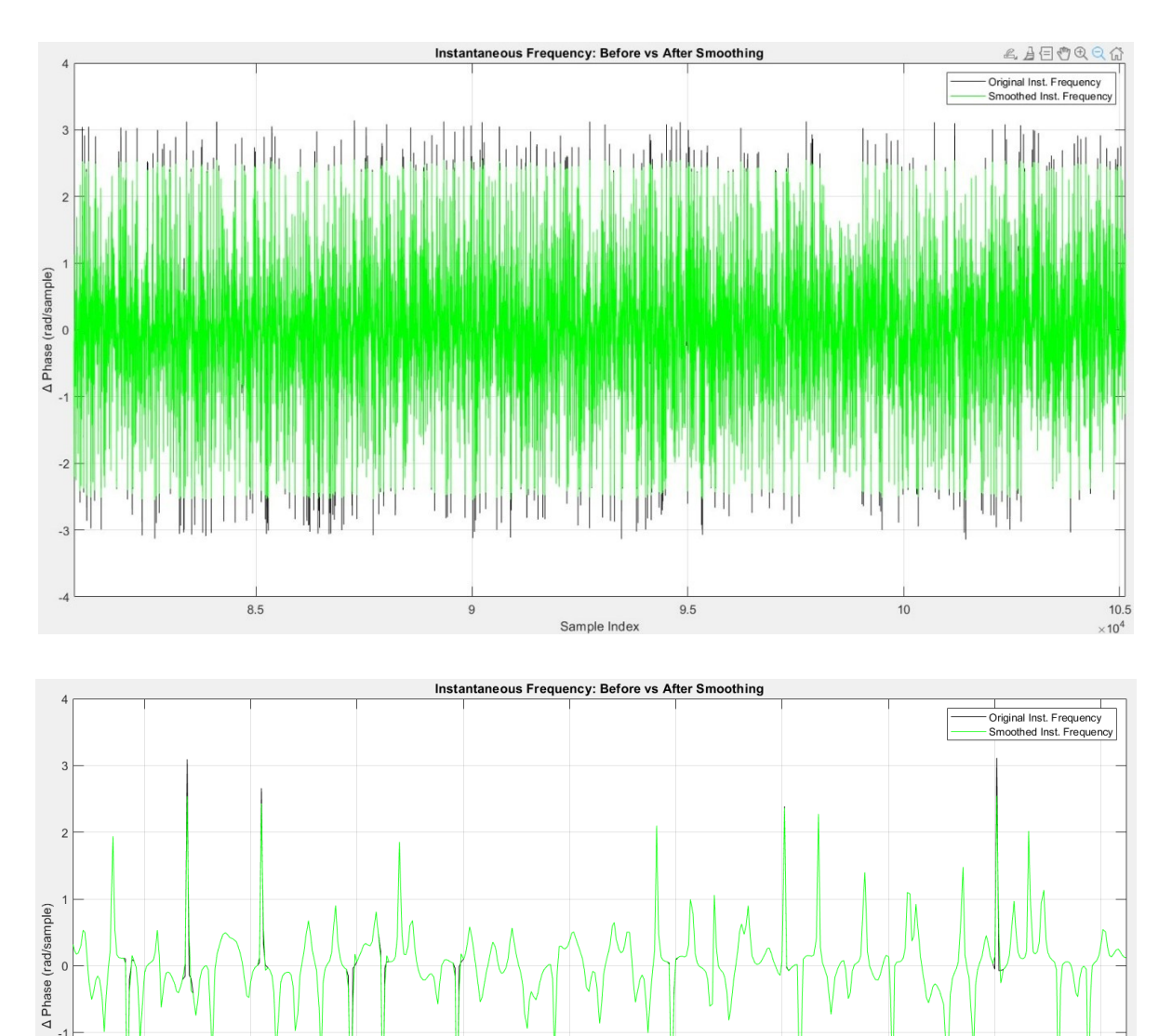


Figure 22: Instantaneous frequency comparison - Threshold = $3\pi/4$

3.3229

3.32295

3.323

3.32305

3.3231

The PSD comparison in Fig. 23 highlights the spectral consequences of smoothing. While the original signal remains well confined within the 802.11a spectrum mask, the smoothed signal exhibits a rise in out-of-band energy due to redistribution of phase excess. This trade-off is a direct consequence of enforcing smoother transitions in the time domain, which inevitably spreads spectral energy.

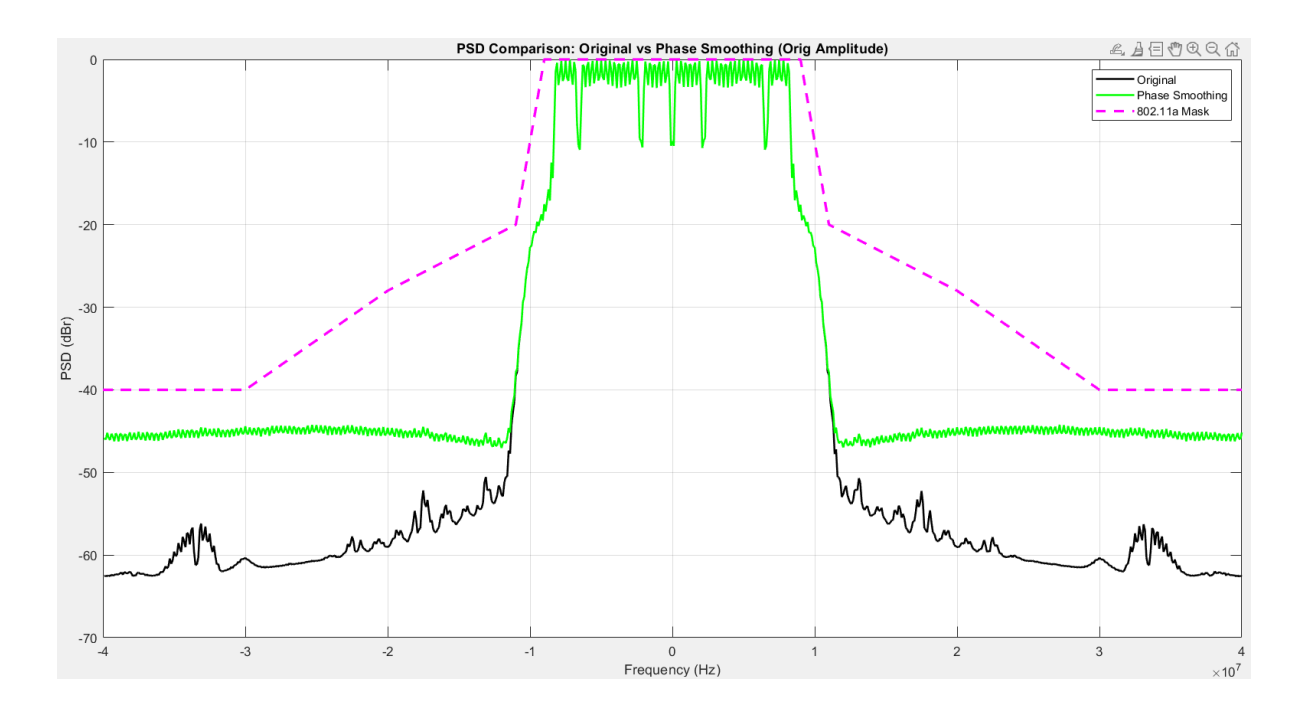


Figure 23: PSD comparison - Threshold = $3\pi/4$

The corresponding error vector magnitude (EVM) and peak-to-average power ratio (PAPR) results are summarized in Table 10. The PAPR remains unchanged (11.36 dB), since phase-domain processing does not alter the amplitude envelope. However, the EVM degrades from –57.47 dB for the original signal to –51.63 dB after smoothing, reflecting the in-band distortion introduced by phase redistribution.

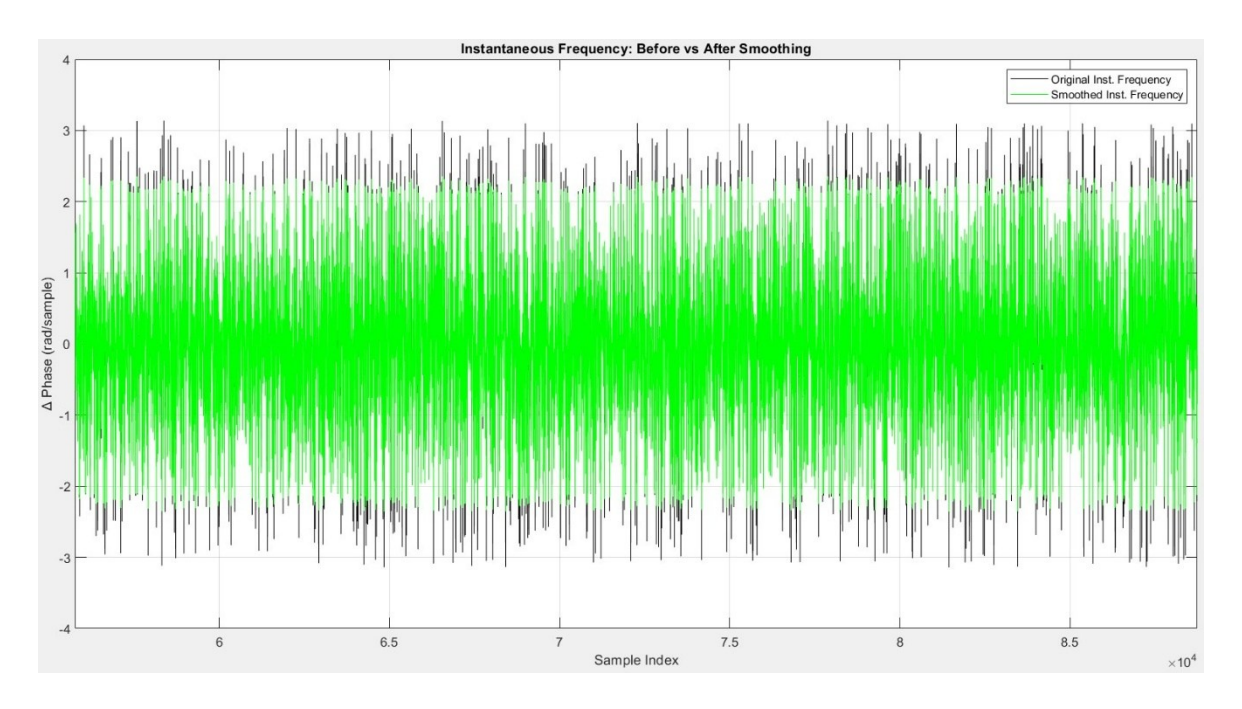
Metric	Original Signal	Phase Smoothed
EVM (dB)	-57.47	-51.63
PAPR	11.36	11.36

Table 10

Overall, with a threshold of $3\frac{\pi}{4}$, phase smoothing effectively suppresses sharp frequency spikes and improves phase continuity, but at the cost of reduced modulation accuracy and an increase in spectral regrowth.

Case 2: Threshold = $2\frac{\pi}{3}$

Fig. 24 and Fig. 25 illustrate the effect of phase smoothing with a threshold of $2\frac{\pi}{3}$. The instantaneous frequency plot in Fig. 24 highlights the significant reduction of sharp frequency spikes compared to the original signal.



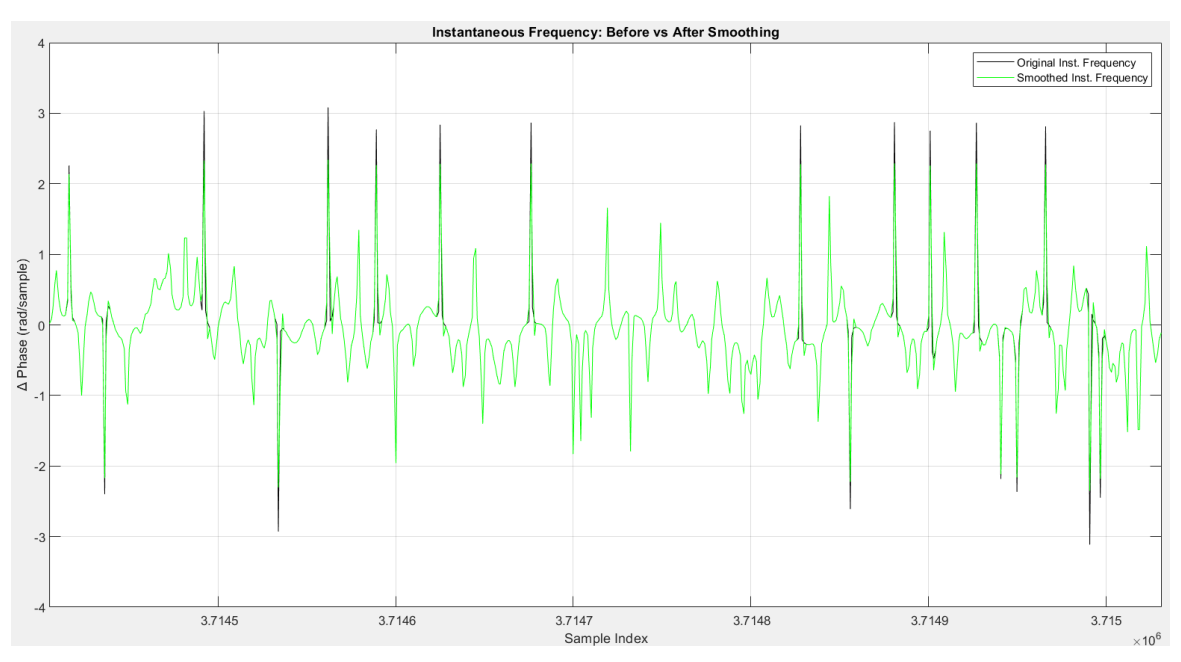


Figure 24:Instantaneous frequency comparison - Threshold = $2\pi/3$

In the power spectral density (PSD) comparison shown in Fig. 25, the smoothed signal exhibits lower spectral sidelobes than the original, improving spectral containment with respect to the IEEE 802.11a mask.

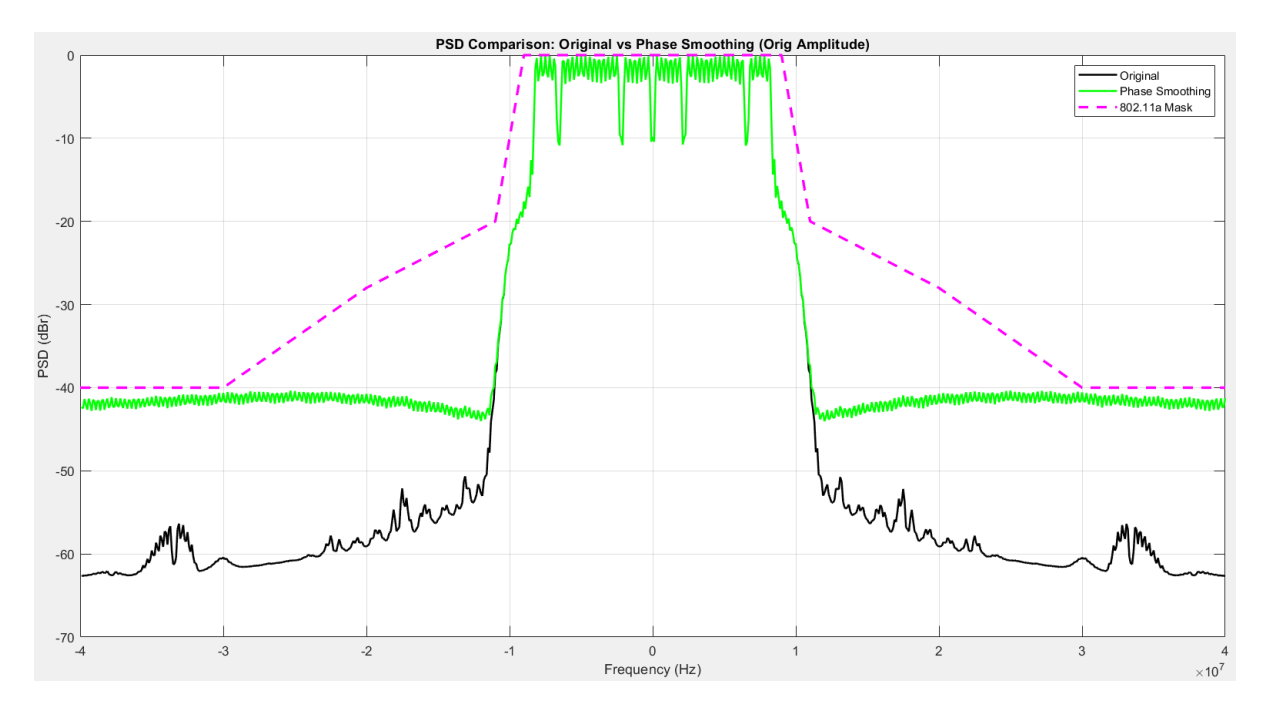


Figure 25:PSD comparison - Threshold = $2\pi/3$

The quantitative performance metrics are summarized in Table 11. Compared to the original signal, which achieves an EVM of –57.47 dB and a PAPR of 11.48 dB, the smoothed signal records an EVM of –48.35 dB while maintaining the same PAPR (11.48 dB). These results confirm that phase smoothing does not affect PAPR, as it operates only on the phase component, but it introduces some degradation in EVM due to phase distortion.

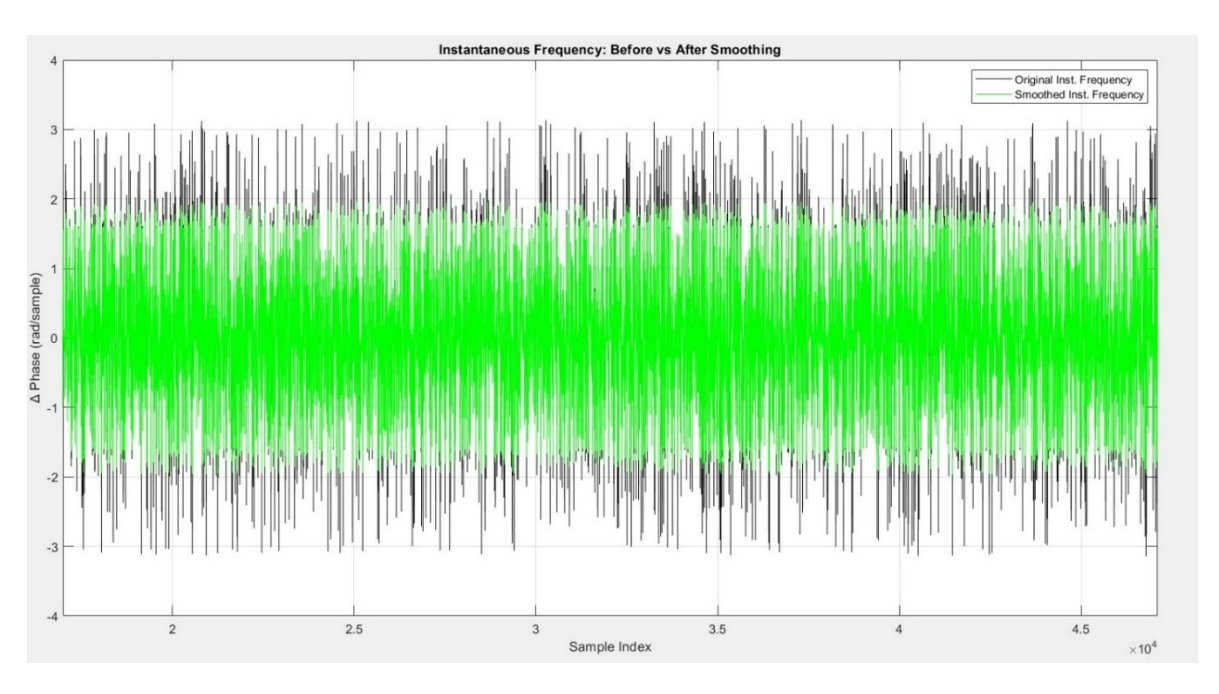
Metric	Original Signal	Phase Smoothed
EVM(dB)	-57.47	-48.35
PAPR	11.48	11.48

Table 11

Overall, applying phase smoothing with a threshold of $2\frac{\pi}{3}$ strikes a balance between preserving PAPR and mitigating spectral regrowth. Although EVM degradation is more pronounced compared to the higher threshold case $(3\frac{\pi}{4})$, the spectral containment benefits are significant, indicating that lower thresholds enhance suppression of frequency-domain sidelobes at the cost of in-band fidelity.

Case 3: Threshold = $\frac{\pi}{2}$

Fig. 26 illustrates the instantaneous frequency before and after applying phase smoothing. At this tighter threshold, a larger number of phase jumps are detected and corrected, leading to a visibly smoother frequency trajectory. The correction mechanism effectively mitigates sharp spikes that originate from phase discontinuities near I/Q zero crossings, thus improving phase continuity.



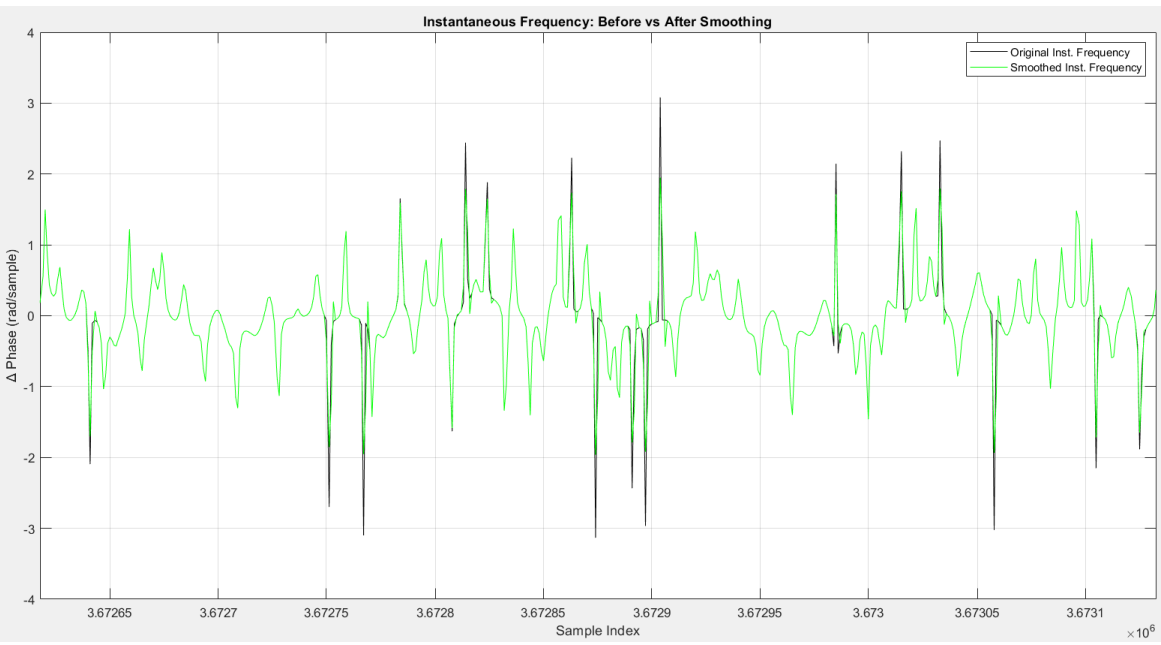


Figure 26:Instantaneous frequency comparison - Threshold = $\pi/2$

Fig. 27 presents the power spectral density (PSD) comparison between the original and smoothed signals. The results show that smoothing reduces high-frequency fluctuations caused by abrupt phase transitions, thereby lowering spectral regrowth. However, this improvement comes at the expense of increased distortion within the useful signal band, as indicated by a shift in the PSD floor.

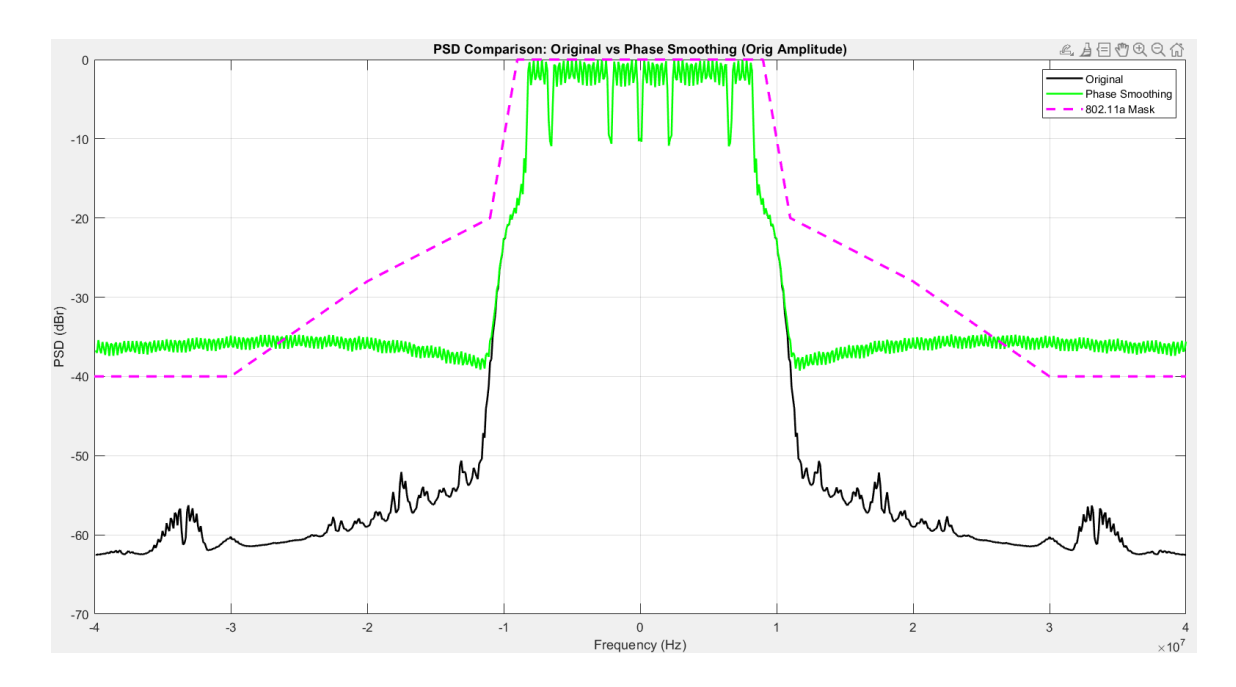


Figure 27:PSD comparison - Threshold = $\pi/2$

Table 12 reports the error vector magnitude (EVM) and peak-to-average power ratio (PAPR). The PAPR remains unchanged at 11.40 dB for both the original and smoothed signals, confirming that phase smoothing does not impact peak amplitudes. On the other hand, the EVM degrades from – 57.50 dB to –42.69 dB due to the stronger modifications introduced to the phase trajectory.

Metric	Original Signal	Phase Smoothed
EVM (dB)	-57.50	-42.69
PAPR	11.40	11.40

Table 12

5.3 Integrated CFR and Phase Smoothing Chain

In the final stage of the MATLAB simulation chain, Peak Windowing and Phase Smoothing were combined to jointly address the two main impairments of polar transmitter architectures: the high peak to average power ratio (PAPR) in the amplitude path and abrupt phase discontinuities in the phase path.

Peak Windowing operates on the amplitude sequence by applying a Hamming-window-based correction to samples exceeding a predefined threshold. In this case, the threshold was set to 0.22. Unlike simple clipping, this method redistributes excess energy across neighbouring samples, thereby reducing spectral regrowth and improving compliance with regulatory spectral masks.

In parallel, the phase trajectory is monitored for discontinuities. When a wrapped phase difference exceeds the threshold, here set to $2\frac{\pi}{3}$, the excess is redistributed across three consecutive samples with weights of $\frac{1}{4}$, $\frac{1}{2}$, and $\frac{1}{4}$. This redistribution smooths the instantaneous frequency, preventing sharp spikes that would otherwise contribute to out-of-band emissions, while preserving total phase continuity.

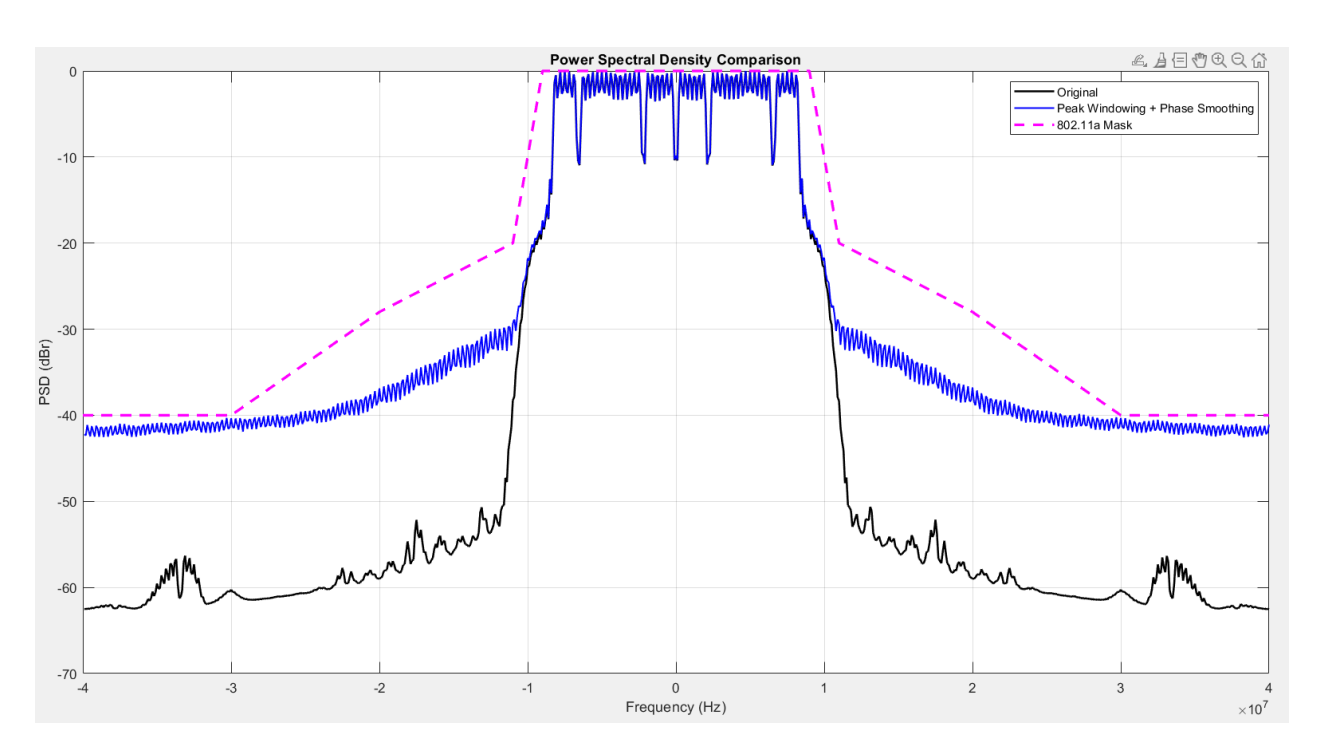


Figure 28:PSD Plot of Integrated scheme

Fig. 28 shows the power spectral density comparison between the original OFDM signal and the processed signal with integrated Peak Windowing and Phase Smoothing. The processed signal exhibits significant suppression of spectral sidelobes and demonstrates strong compliance with the IEEE 802.11a spectrum mask.

The quantitative results in Table 13 confirm these improvements. The integrated approach reduces the PAPR from 11.94 dB in the original signal to 6.28 dB, while the EVM increases from -57.47 dB to -26 dB due to the combined in-band distortion introduced by amplitude correction and phase redistribution.

Metric	Original Signal	P.W & Phase Smoothing
EVM(dB)	-57.47	-26
PAPR	11.94	6.28

Table 13

Additional spectral measurements reported in Table 14 further illustrate the improvement. At offset frequencies of 11 MHz, 20 MHz, and 30 MHz, the processed signal shows a reduction of approximately 18–20 dB relative to the original. This highlights the robustness of the combined method in suppressing out-of-band radiation and maintaining spectral containment.

Frequency (MHz)	Original Signal	P.W & Phase Smoothing
11	-38.362	-29.337
20	-58.978	-36.765
30	-60.267	-40.316

Table 14

Overall, the integration of Peak Windowing and Phase Smoothing provides a balanced solution: PAPR is substantially reduced, out-of-band emissions are strongly suppressed, and EVM remains within the acceptable limits defined by IEEE 802.11a, ensuring regulatory compliance.

6 CHAPTER 6: RTL Implementation of Key Modules

The previous chapter presented the MATLAB simulation chain, where the proposed predistortion techniques were modelled and validated at algorithmic level. While this analysis confirmed the effectiveness of the methods in terms of PAPR reduction, EVM performance, and spectral compliance, it remained abstracted from the timing and hardware constraints of a real implementation.

In this chapter, the focus shifts to the RTL description of the key building blocks forming the polar modulator chain. Each module, the CORDIC converter, the Crest Factor Reduction block, and the Phase Smoothing unit was designed in Verilog HDL using a synchronous, pipelined architecture. Fixed-point arithmetic, rounding, and saturation were applied consistently with the MATLAB models to ensure bit-true comparability. Verification was performed through dedicated testbenches, where MATLAB-generated stimuli and reference outputs allowed a direct, sample by sample comparison with the RTL implementation.

6.1 RTL Implementation of CORDIC

6.1.1 Architecture and Block Diagram

The Cartesian-to-polar conversion is implemented through a vectoring-mode CORDIC algorithm. The architecture was designed as a fully pipelined structure, enabling continuous real-time processing with one output sample per clock cycle after pipeline filling. Fig. 29 illustrates a simple block diagram of the CORDIC module.

The data path can be divided into three main parts. In the pre-processing stage, the signed inputs are first scaled by a constant factor to improve intermediate precision. When the input abscissa is negative, both Cartesian components are inverted so that the core always processes values with non-negative x. A flag is propagated in parallel with the data to enable quadrant correction at the output.

The iterative core consists of sixteen micro-rotation stages. At each iteration the vector is conditionally rotated by an angle of arctan(2⁻ⁱ), obtained from a fixed lookup table. The decision is based on the sign of the current ordinate, following the vectoring-mode principle. Each stage updates the Cartesian components and the accumulated phase using only additions, subtractions, and rounded binary shifts. Pipeline registers separate all stages, ensuring a short combinational delay and high maximum frequency.

In the output stage, the final accumulated phase and magnitude are combined with the delayed original inputs to resolve special axis cases. Explicit rules are applied when one of the coordinates is zero, guaranteeing deterministic results for angles on the axes. If the input vector was pre-flipped at the beginning, a quadrant correction of $\pm \pi$ is added. The internal phase accumulator operates in

Q1.15 format and is later converted to Q3.13, while the magnitude is corrected for the intrinsic CORDIC gain and delivered in the chosen fixed-point format.

Overall, the design introduces a latency of seventeen cycles, corresponding to the initial register, the sixteen iterative stages, and the final output register. Once the pipeline is filled, the circuit sustains a throughput of one sample per clock.

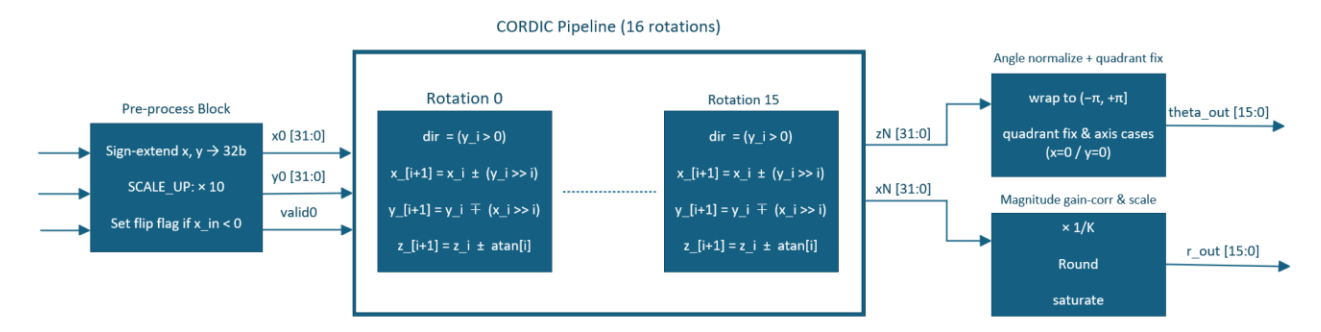


Figure 29: RTL Block Diagram – CORDIC (16 rotations)

6.1.2 Input/Output Specification and Fixed-Point Representation

Inputs and outputs of the designed module is illustrated in table 15. The input Cartesian components are represented in Q3.13 format, which offers a good compromise between dynamic range and precision for the normalized OFDM signal. The output magnitude is also expressed in Q3.13 but scaled by a constant factor to account for the initial pre-scaling. The output phase is provided in Q3.13, spanning the interval $(-\pi, +\pi]$, with $-\pi$ mapped to the most negative representable value.

Internally, the CORDIC stages use 32-bit accumulators for the Cartesian variables and a Q1.15 representation for the phase accumulator. The lookup table of elementary angles is stored in the same Q1.15 format. To improve numerical accuracy, all right shifts are performed with rounding to the nearest integer, and all final outputs are saturated to the 16-bit range.

The interface is synchronous, and register based. A validity signal accompanies the input and propagates through the pipeline, ensuring that outputs are always aligned with their corresponding inputs. The reset condition clears all registers, allowing deterministic restart of the pipeline.

Signal	Direction	Format	Description
clk	INPUT	1 bit	Global clock signal driving the pipeline stages
rst	INPUT	1 bit	reset that initializes all pipeline registers
valid_in	INPUT	1 bit	Indicates the presence of a valid input sample.
x_in	INPUT	16-bit	In-phase Cartesian component of the input signal in Q3.13 format.
y_in	INPUT	16-bit	Quadrature Cartesian component of the input signal in Q3.13 format.
valid_out	OUTPUT	1 bit	Indicates that the outputs are valid (after pipeline latency).
theta_out	OUTPUT	16-bit	Phase of the input vector, mapped to the $(-\pi, +\pi)$ range in Q3.13 format.
r_out	OUTPUT	16-bit	Magnitude of the input vector, normalized and scaled by factor 10 in Q3.13 format.

Table 15: Input / Outputs to CORDIC

6.2 RTL Implementation of CFR

6.2.1 Architecture and Block Diagram

The crest factor reduction block implements a window-based peak-cancellation scheme. The input magnitude (Q3.13 with an overall ×10 scaling) is compared against a programmable threshold in the same format. Any excess above the threshold is converted into a correction seed, while samples below the threshold produce zero correction. A four-sample delay line in the main path preserves alignment between the unmodified signal and the centre of the subsequent correction window.

The correction seeds are fed to a nine-tap symmetric FIR with fixed Hamming coefficients stored in Q1.15. The FIR is realized with a 9-element shift register (correction history) and a multiply–accumulate data path; partial products ($16 \times 16 \rightarrow 32$) are sign-extended and summed to a 40-bit internal accumulator. To obtain a properly scaled correction pulse, the accumulator is rounded to nearest by adding a bias of 2^{14} and shifting right by 15 bits. The delayed input sample is then subtracted by this rounded correction, and the result is saturated to the non-negative 16-bit range [0, 32767], ensuring that the amplitude never goes below zero. The output preserves the input's fixed-point format (Q3.13×10).

The design is lightly pipelined to sustain one sample per clock once filled. The FIR sum is latched for use in the next cycle, and the input path includes the four-sample delay plus an alignment register, resulting in an overall latency of approximately five cycles while maintaining a throughput of one output per cycle. Figure 30 shows the main blocks: comparator/correction generation, nine-tap Hamming FIR, rounding and scaling, the aligned delay line, and the final subtraction with saturation.

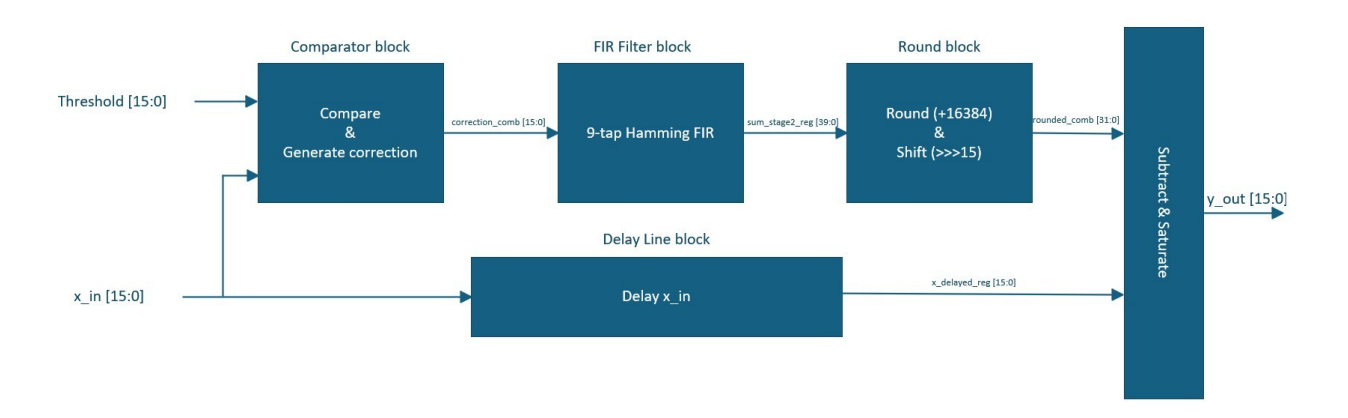


Figure 30: RTL Block Diagram - Crest Factor Reduction

6.2.2 Input/Output Specification and Fixed-Point Representation

All external signals are represented in Q3.13 fixed-point format with the same scaling factor used consistently across the transmission chain (Table 16). The input magnitude and the threshold share this representation, while the output magnitude is saturated to the interval [0, 32767] to avoid negative values after correction. The Hamming coefficients used by the filter are stored in Q1.15 format. Each correction value is multiplied by its coefficient, producing 32-bit intermediate results that are accumulated with sufficient headroom to prevent overflow. After accumulation, the result is rounded and shifted back into the Q3.13 domain before subtraction from the delayed input sample.

The subtraction result is saturated to fit into the 16-bit output format. Negative values are clipped to zero, while positive values exceeding the representable range are limited to the maximum. The module operates synchronously with the system clock and produces one output per cycle after an initial latency of four cycles. Verification was carried out by stimulating the implementation with test sequences generated in MATLAB and comparing the outputs on a sample-by-sample basis. Test cases included isolated peaks, consecutive peaks, and values close to the threshold, confirming that the hardware reproduces the reference behaviour with correct window alignment and consistent rounding.

Signal	Direction	Format	Description
clk	INPUT	1 bit	Global clock signal driving the pipeline stages
rst	INPUT	1 bit	reset that initializes all pipeline registers
x_in	INPUT	16-bit	Magnitude input sample in Q3.13 format with scaling factor applied.
threshold	INPUT	16-bit	Programmable threshold value in Q3.13 format with the same scaling as the input.
y_out	OUTPUT	16 bit	Corrected magnitude sample in Q3.13 format after window-based peak cancellation. Saturated to the range [0, 32767].
ready	OUTPUT	1 bit	Constant high signal indicating that the module is always able to accept new input samples.

Table 16: Input / Outputs to CFR

6.3 RTL Implementation of Phase Smoothing

6.3.1 Architecture and Block Diagram

The phase smoothing unit mitigates abrupt phase transitions by redistributing only the excess portion of a wrapped phase jump over a short temporal window. All signals are represented in Q3.13 fixed point. The block maintains a sliding window of three consecutive phase samples (oldest to newest). Once the window is filled, the wrapped phase increment between the first two samples is computed in the interval $(-\pi, \pi]$. This wrapping prevents normal crossings of $\pm \pi$ from being misinterpreted as large discontinuities and keeps the comparison invariant to absolute phase.

The wrapped increment is compared to a programmable threshold in the same numeric format. If the magnitude is below threshold, the window is passed through unchanged. When the magnitude exceeds the threshold, only the surplus beyond the threshold is processed. The surplus is partitioned deterministically into one half, one quarter, and the remaining quarter using arithmetic shifts, which are hardware-efficient and avoid multipliers. These portions are then applied symmetrically across the three samples: a positive adjustment is added to the oldest sample (approximately $+\frac{1}{4}$ of the excess), a negative adjustment is applied to the middle sample $(-\frac{1}{2})$, and a positive remainder is added to the newest sample $(+\frac{1}{4})$. In this way, the total phase across the window is preserved while the instantaneous frequency spike is spread in time and reduced in amplitude.

At each clock cycle, once the window is full, the (possibly corrected) oldest sample is emitted, the window shifts by one position, and the new input is inserted. When the input stream ends, a flush mechanism drains the remaining samples in the buffer so that no data is dropped. After the initial fill, the design delivers one output per clock; the observable latency equals the window depth. The threshold is fully programmable, enabling the same hardware to operate from conservative to aggressive smoothing settings without architectural changes.

Figure 31 summarizes the data path: a three-sample window buffer and wrap-to- $(-\pi, \pi]$ stage; threshold comparison and excess extraction; deterministic split of the excess into half/quarter/remainder; symmetric application of the corrections; and the registered output with valid handshaking.

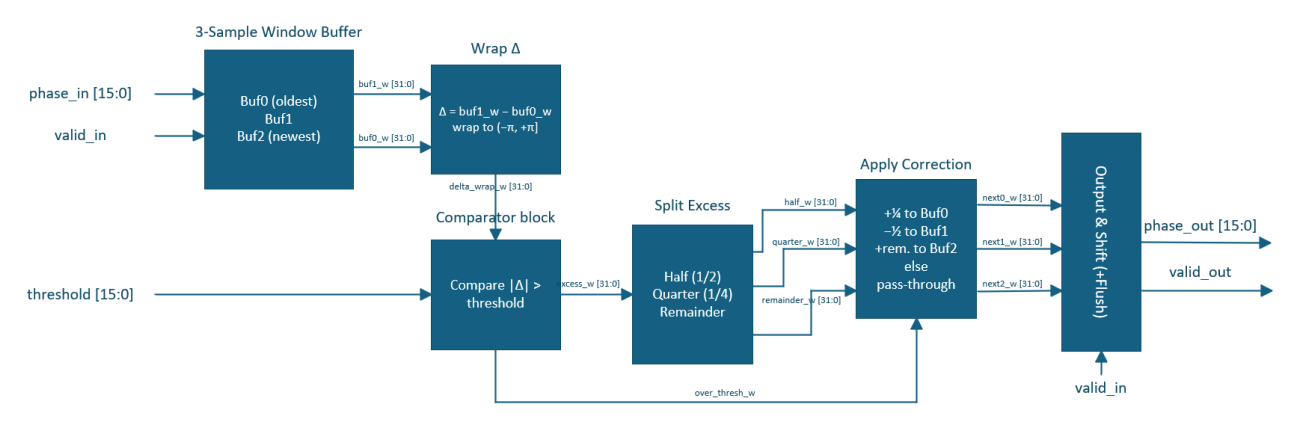


Figure 31: RTL Block Diagram – Phase Smoothing

6.3.2 Input/Output Specification and Fixed-Point Representation

Input and output phases use Q3.13, covering $(-\pi, +\pi]$. Internal arithmetic employs sign-extended 32-bit intermediates to accommodate wrapping, threshold comparison, and redistribution with ample headroom. The wrap operation maps the raw difference into $(-\pi, +\pi]$ by adding or subtracting 2π as required. Excess splitting is implemented with arithmetic right shifts (floor division in fixed-point), providing deterministic half/quarter partitions. The corrected output sample is returned to Q3.13 by truncation to 16 bits with sign, consistent with the rest of the chain. The interface is synchronous with a valid-only streaming handshake: a valid input may be accepted every clock; after the third input (window full), one corrected output is produced per cycle in steady state. The first valid output appears on the third input sample, and the throughput is one sample per clock thereafter. A flush mode ensures that any remaining buffered samples are emitted; applying the same correction rules when the window is still full. So, no data are lost at stream boundaries. Reset clears all state, yielding a deterministic restart.

Signal	Direction	Format	Description
clk	INPUT	1 bit	Global clock signal driving the pipeline stages
rst	INPUT	1 bit	reset that initializes all pipeline registers
valid_in	INPUT	1 bit	Indicates that the input phase sample is valid.
phase_in	INPUT	16-bit	Input phase sample in Q3.13 format, wrapped to the interval (–π, +π].
threshold	INPUT	16-bit	Programmable threshold in Q3.13 format, defining the maximum allowed phase increment before smoothing is applied.
valid_out	OUTPUT	1 bit	Indicates that the output phase sample is valid. The first valid output appears after the third input sample.
phase_out	OUTPUT	16-bit	Smoothed output phase sample in Q3.13 format, corrected when excess increments are detected, otherwise passed through unchanged.

Table 17: Input / Outputs to Phase Smoothing

7 CHAPTER 7: Results and Evaluation

7.1 MATLAB Results

7.1.1 PAPR Reduction Methods – Amplitude Clipping and Peak Windowing

In the amplitude path, two peak-reduction techniques were investigated: amplitude clipping and peak windowing. Both techniques operate after interpolation and leave the phase trajectory unchanged.

Amplitude clipping is a straightforward approach where signal magnitudes exceeding a predefined threshold are truncated. This method achieves significant PAPR reduction, but the abrupt non-linearity introduces in-band distortion, which degrades modulation accuracy, and generates out-of-band components, which increase spectral regrowth.

Peak windowing addresses these drawbacks by redistributing excess amplitude energy instead of discarding it. When a sample exceeds the threshold, a correction term is generated and shaped using a Hamming window before being subtracted from the original signal. This smoother suppression reduces spectral leakage at the expense of slightly higher in-band distortion compared to clipping.

The performance of the two techniques was analysed at three threshold values: 0.28, 0.22, and 0.17. At higher thresholds, both methods achieve moderate PAPR reduction while preserving very low EVM. Clipping maintains better modulation accuracy, whereas peak windowing demonstrates superior suppression of far-out spectral components, particularly beyond 20 MHz. At intermediate thresholds, PAPR is further reduced, with clipping continuing to achieve lower EVM and windowing providing better spectral containment. At the lowest threshold, both methods achieve PAPR values close to 6 dB, but at the cost of degraded EVM. Even in this case, peak windowing consistently ensures better compliance with the spectral mask by reducing out-of-band emissions more effectively than clipping.

Overall, amplitude clipping is advantageous when preserving in-band fidelity is the primary objective, while peak windowing provides better spectral containment and regulatory compliance. The choice between the two methods depends on the acceptable trade-off between modulation accuracy and out-of-band suppression.

7.1.2 Phase Smoothing

In the phase path, the main impairment arises from abrupt discontinuities produced by the conversion from Cartesian to polar coordinates. These discontinuities result in instantaneous frequency spikes that degrade spectral containment and increase the stress on phase-locked loops (PLLs). To mitigate this issue, a phase smoothing algorithm was implemented.

The algorithm monitors the difference between consecutive phase samples. When a discontinuity exceeding a predefined threshold is detected, the excess is redistributed across three consecutive samples according to fixed ratios of $\frac{1}{4}$, $\frac{1}{2}$, and $\frac{1}{4}$. This redistribution suppresses sharp jumps while preserving the total accumulated phase, ensuring that the integrity of the transmitted information is maintained.

The performance of the algorithm was evaluated at three thresholds: $3\frac{\pi}{4}$, $2\frac{\pi}{3}$, and $\frac{\pi}{2}$. For the highest threshold $(3\frac{\pi}{4})$, the method provided effective suppression of spectral spikes while introducing only a moderate increase in error vector magnitude (EVM). At the intermediate threshold $(2\frac{\pi}{3})$, stronger smoothing was achieved, further reducing spectral regrowth at the cost of a higher EVM penalty. At the lowest threshold $(\frac{\pi}{2})$, the algorithm aggressively redistributed phase jumps, resulting in substantial EVM degradation and partial violation of the IEEE 802.11a spectrum mask.

These results highlight the fundamental trade-off of phase smoothing: higher thresholds preserve modulation accuracy but leave residual spectral spikes, while lower thresholds improve spectral containment but risk excessive in-band distortion. An intermediate threshold therefore offers the best compromise, ensuring compliance with both spectral mask and modulation accuracy requirements.

7.1.3 Integration of Peak Windowing and Phase Smoothing

In the final stage of MATLAB analysis, the two techniques were integrated to jointly mitigate the main impairments of polar transmitters: the high peak-to-average power ratio (PAPR) in the amplitude path and abrupt phase discontinuities in the phase path. Peak windowing was applied with a threshold of 0.22, while phase smoothing was configured with a threshold of $2\frac{\pi}{3}$. Moreover, the instantaneous frequency plot confirms the effectiveness of the smoothing stage in reducing large phase jumps, ensuring a more uniform frequency trajectory. At the same time, the amplitude peaks are suppressed through window-based redistribution, thereby addressing the two impairments simultaneously.

Quantitative performance metrics are reported in Table 13. The integrated method lowers the PAPR from 11.94 dB in the original signal to 6.28 dB, a reduction comparable to that achieved by peak windowing alone. The EVM, however, increases from -57.47 dB to -26 dB, reflecting the combined in-band distortion introduced by amplitude and phase-domain processing. Despite this increase, the EVM remains within the acceptable IEEE 802.11a limit of -16 dB.

The improvement in spectral containment is evident in the PSD comparison of Figure 28. Out-of-band emissions are substantially reduced, with measured PSD values at 11 MHz, 20 MHz, and 30 MHz showing reductions of approximately 18–20 dB relative to the original signal (Table 14). This demonstrates the robustness of the integrated approach in suppressing out-of-band radiation and ensuring compliance with the IEEE 802.11a spectrum mask.

Overall, the integration of peak windowing and phase smoothing provides a balanced solution. While the EVM degradation is higher than in the case of individual methods, the joint processing achieves substantial PAPR reduction and superior spectral containment, fulfilling both regulatory and performance requirements.

7.2 RTL Results

The RTL implementation of the complete transmit chain was synthesized and evaluated at two frequency targets (table 18). The primary case of interest is 100 MHz, which corresponds to the conditions assumed in the MATLAB simulations. A higher target of 160 MHz was also considered to assess the scalability of the design.

At 100 MHz, the design closes timing with a comfortable setup margin. The critical path is located within the vector-rotation stage, which is consistent with the depth of its computational pipeline. At 160 MHz, timing closure is also achieved, with a positive though narrower slack. In this case, the critical path shifts towards the phase-smoothing stage, reflecting the more demanding clock period and the accumulation depth of this block. Importantly, in both scenarios the design satisfies timing requirements, confirming the robustness of the chosen architecture.

Frequency (MHz)	Clock Period(ns)	Required Time(ns)	Data Arrival(ns)	Setup Slack (ns)
100	10	8.9431	8.6641	0.2790
160	6.25	5.5708	5.4987	0.0721

Table 18: Timing Summary

The synthesis results also provide insight into the area distribution across the main blocks of the chain (Table 19). The CORIDC module dominates, contributing approximately 81-82 % of the total cell area at both frequencies. Peak windowing accounts for about 13 %, while the phase-smoothing stage represents around 6 %. The total cell area increases only modestly, from 4712 μ m² at 100 MHz to 4805 μ m² at 160 MHz, corresponding to an overhead of roughly 2 %. This small increase is attributed to additional buffering and cell upsizing required to sustain the higher operating frequency and remains within typical expectations for such a frequency step.

Frequency (MHz)	Total Cell Area	CORDIC	P. Windowing	Phase Smoothing
100	4712.04	3836 (81.4%)	602.06 (12.8%)	268.33 (5.7%)
160	4804.77	3918 (81.6%)	603.23 (12.6%)	277.28 (5.8%)

Table 19: Area Summary and block-level distribution

The synthesis results also provide insight into the area distribution across the main blocks of the chain. As illustrated in table 19, the CORDIC stage dominates, contributing approximately 81-82% of the total cell area at both frequencies. Peak windowing accounts for about 13 %, while the phase-smoothing stage represents around 6 %. The total cell area increases only modestly, from $4712 \ \mu m^2$ at $100 \ MHz$ to $4805 \ \mu m^2$ at $160 \ MHz$, corresponding to an overhead of roughly 2 %. This small increase is attributed to additional buffering and cell upsizing required to sustain the higher operating frequency and remains within typical expectations for such a frequency step.

7.3 MATLAB vs RTL Comparison

The final step of the evaluation consists in comparing the MATLAB simulation results with the corresponding RTL implementation of the full transmit chain. This comparison validates both the algorithmic correctness and the hardware feasibility of the proposed design. Fig. 32 reports the power spectral density (PSD) of the original OFDM signal, the MATLAB-based crest factor reduction (CFR) chain, and the RTL implementation of the same processing. The MATLAB and RTL curves are visually indistinguishable, demonstrating that the hardware modules reproduce the algorithmic behaviour with high fidelity. Both implementations ensure compliance with the IEEE 802.11a spectral mask while achieving significant suppression of out-of-band emissions compared to the unprocessed signal.

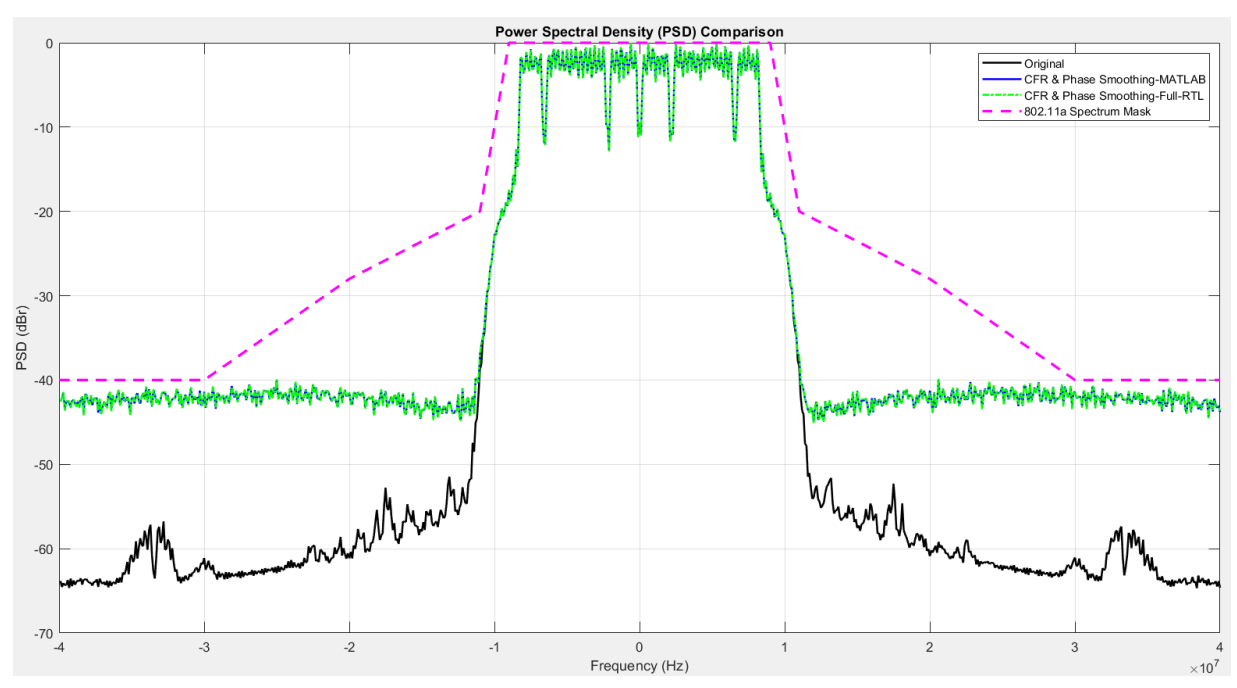


Figure 32: PSD plot - Original Signal, Full Chain: MATLAB/RTL

Table 20 summarizes the numerical results of the comparison. The MATLAB chain reduces the PAPR from 10.72 dB in the original signal to 8.53 dB, while the EVM increases from -56.81 dB to -39.48 dB due to the non-linear operations of CFR. The RTL implementation achieves identical values, confirming complete functional equivalence with the MATLAB reference. Additional power checks further reinforce this equivalence: the RTL chain introduces a negligible scaling difference of -0.01 dB between input and output, and the final power ratio between the RTL and MATLAB CFR outputs is 0.00 dB. These results confirm that the fixed-point hardware implementation preserves both the amplitude scaling and the average signal power of the floating-point MATLAB model.

Frequency (MHz)	EVM(dB)	PAPR
Original	-56.81	10.72
Full Chain - MATLAB	-39.48	8.53
Full Chain - RTL	-39.48	8.53

Table 20

Overall, the comparison establishes that the RTL design faithfully reproduces the MATLAB reference in terms of PAPR reduction, EVM degradation, and spectral containment. This alignment validates the proposed architecture as a suitable candidate for real-time implementation while ensuring consistency across simulation and hardware domains.

8 CHAPTER 8: Conclusions and Future Work

8.1 Summary of Achievements

This thesis has presented the design, implementation, and evaluation of a digital polar transmitter chain for OFDM signals, focusing on the two most critical aspects of polar-domain processing: crest factor reduction (CFR) in the amplitude path and phase smoothing in the phase path. Both MATLAB-based algorithmic models and their corresponding RTL implementations were developed, verified, and compared, ensuring functional equivalence and performance consistency.

On the amplitude side, a window-based CFR technique was implemented using a thresholding comparator, a short Hamming-window FIR filter, and subtraction with saturation. This approach demonstrated effective suppression of signal peaks while maintaining compliance with modulation accuracy and spectral containment requirements. The RTL design was validated against the MATLAB reference, showing identical outputs in terms of PAPR, EVM, and PSD performance.

On the phase side, a threshold-driven smoothing algorithm was introduced to mitigate abrupt phase jumps, which otherwise cause instantaneous frequency spikes and spectral regrowth. The algorithm redistributed the excess phase beyond a programmable threshold across a three-sample window in fixed ratios, thereby preserving the overall accumulated phase while reducing spectral leakage. The RTL version reproduced the MATLAB results with cycle-by-cycle equivalence, including preservation of total phase, power normalization, and compliance with IEEE 802.11a mask requirements.

A complete MATLAB–RTL co-simulation flow was established, enabling direct comparison between the behavioural model and the hardware implementation across all processing stages. Quantitative evaluation confirmed that the RTL chain achieves the same performance as the MATLAB reference, with EVM and PAPR improvements closely matching. Post-synthesis results further confirmed that the architecture supports the required operating frequency of 100 MHz; the main design target defined in MATLAB simulations, while still sustaining operation at 160 MHz.

8.2 Future Directions

Although the present work has delivered a functional and verified design, several avenues remain open for further improvement and exploration:

1. Advanced CFR and peak-reduction strategies

• The current CFR relies on fixed Hamming-window shaping. Future work could investigate adaptive windowing, peak cancellation, or hybrid CFR-clipping schemes to further optimize the trade-off between EVM and spectral containment.

2. Improved phase smoothing algorithms

• The deterministic half/quarter redistribution rule is efficient but rigid. Alternative redistribution strategies, possibly adaptive to the magnitude or frequency of phase jumps, could reduce EVM penalties while maintaining mask compliance.

3. CORDIC optimization

• Although the implemented CORDIC pipeline is functionally correct and efficient, further optimization is possible through radix-4 iterations, angle recoding, or hybrid LUT-CORDIC approaches, reducing latency and area while preserving accuracy.

4. Applicability to next-generation standards

• While this thesis was based on IEEE 802.11a parameters, the methods are generalizable. Evaluating the proposed architecture under 5G/6G waveform conditions (e.g., OFDM with higher subcarrier densities, FBMC, or filtered-OFDM) would highlight scalability and robustness across modern wireless standards.

9 References

- [1] Alan V. Oppenheim and George C. Verghese, Chapter 12: "Pulse Amplitude Modulation (PAM) and Quadrature Amplitude Modulation (QAM)", 2010.
- [2] Y. Chai, "Performance Analysis of QAM Modulation and Demodulation, Highlights in Science, Engineering and Technology", vol. 134, pp. 114–125, 2025.
- [3] Muhammad A. Tariq, "Quantitative Evaluation of High Speed Microwave Modem", master's Thesis, Chalmers University of Technology, 2011.
- [4] IEEE Draft Standard for Information Technology "Telecommunications and Information Exchange Between Systems Local and Metropolitan Area Networks" Specific Requirements Part 11: Wireless LAN Medium Access Control (MAC) and Physical Layer (PHY) Specifications, IEEE P802.11-REVmc/D5.0, Jan. 2016.
- [5] Behrouz Farhang-Boroujeny and Hussein Moradi, "OFDM Inspired Waveforms for 5G", IEEE Communications Surveys & Tutorials, 2016.
- [6] M. R. Beikmirza et al., "A Wideband Energy-Efficient Multi-Mode CMOS Digital Transmitter," IEEE J. Solid-State Circuits, 2023.
- [7] M. R. Beikmirza, "Advanced Bits-In RF-Out Transmitters", Ph.D. Dissertation, Delft University of Technology, 2023.
- [8] Qian, Huizhen; Zhou, Jie; Yang, Bingzheng; Luo, Xun. "A 4-Element Digital Modulated Polar Phased-Array Transmitter With Phase Modulation Phase-Shifting," IEEE Journal of Solid-State Circuits, 2021.
- [9] Shokoufeh Arbabi. "A 2.4 GHz Phase Modulator for a WLAN OFDM Polar Transmitter in 0.18 µm CMOS", Ph.D. Dissertation, Texas A&M University, 2014.
- [10] Zhou B. "A Low-Noise Delta-Sigma Phase Modulator for Polar Transmitters", The Scientific World Journal, 2014.
- [11] P. K. Meher, J. Valls, T.-B. Juang, K. Sridharan, and K. Maharatna, "50 Years of CORDIC: Algorithms, Architectures, and Applications," IEEE Transactions on Circuits and Systems I, vol. 56, no. 9, pp. 1893–1907, Sep. 2009.
- [12] I. Hussain and C. P. Raj, "Design and Implementation of Low Power and High Speed Autocorrelator and CORDIC Architectures for OFDM," IACSIT Int. J. Eng. Technol., vol. 3, no. 3, pp. 315–319, Jun. 2011.
- [13] J. Song and H. Ochiai, "A Low-Complexity Peak Cancellation Scheme and its FPGA Implementation for PAPR Reduction," EURASIP J. Wireless Commun. Netw., 2015:85, 2015.

- [14] Z. Xing et al., "A Hybrid Companding and Clipping Scheme for PAPR Reduction in OFDM Systems", IEEE Access, 2021.
- [15] S. H. Han and J. H. Lee, "An Overview of Peak-to-Average Power Ratio Reduction Techniques for Multicarrier Transmission", IEEE Wireless Communications, 2005.
- [16] H. Ochiai and H. Imai, "On the Distribution of the Peak-to-Average Power Ratio in OFDM Signals", IEEE Transactions on Communications, 2001.
- [17] R. K. Martin and M. Haker, "Reduction of Peak-to-Average Power Ratio in Transform Domain Communication Systems", IEEE Transactions on Wireless Communications, 2009.
- [18] Hamidreza Moazzen, Abbas Mohammadi, Mahdi Majidi, "Performance Analysis of Linear Precoded MU-MIMO-OFDM Systems With Nonlinear Power Amplifiers and Correlated Channel", IEEE Transactions on Communications, 2019.
- [19] Sara R. Biyabani et al., "Energy Efficiency Evaluation of Linear Transmitters for 5G NR Wireless Waveforms", IEEE Transactions on Green Communications and Networking, 2019.
- [20] J. van de Beek and F. Berggren, "N-Continuous OFDM," IEEE Communications Letters, vol. 13, no. 1, pp. 1–3, Jan. 2009.
- [21] J.-W. Lai et al., "A 0.27mm2 13.5dBm 2.4GHz all-digital polar transmitter using 34%-efficiency Class-D DPA in 40nm CMOS," 2013 IEEE International Solid-State Circuits Conference Digest of Technical Papers, San Francisco, CA, USA, 2013, pp. 342-343.
- [22] J. Zhuang, K. Waheed, and R. B. Staszewski, "A Technique to Reduce Phase/Frequency Modulation Bandwidth in a Polar RF Transmitter," IEEE Transactions on Circuits and Systems I, vol. 57, no. 8, pp. 2196–2207, Aug. 2010.
- [23] M. Faulkner, "The Effect of Filtering on the Performance of OFDM Systems," IEEE Transactions on Vehicular Technology, vol. 49, no. 5, pp. 1877–1884, Sept. 2000.
- [24] A. T. Gamage, T. A. Rahman, A. I. Sulyman, and M. H. Rehmani, "Peak-to-Average Power Ratio Reduction in OFDM Systems: A Survey and Taxonomy", IEEE Access, vol. 9, pp. 139513–139544, 2021.
- [25] Olli Vaananen, "DIGITAL MODULATORS WITH CREST FACTOR REDUCTION TECHNIQUES"; master's Thesis, Helsinki University of Technology.
- [26] Vaananen, Olli & Vankka, Jouko & Halonen, K.. (2005). "Simple algorithm for peak windowing and its application in GSM, EDGE and WCDMA systems". Communications, IEE Proceedings-. 152. 357 362. 10.1049/ip-com:20059014.
- [27] L. Wang and C. Tellambura, "A Simplified Clipping and Filtering Technique for PAR Reduction in OFDM Systems", IEEE Transactions on Communications, 2005.

[28] Y. A. Al-Jawhar et al., "Improving PAPR Performance of Filtered OFDM for 5G Communications Using PTS", ETRI Journal, vol. 42, no. 2, pp. 210–220, 2020.